Nomenclature

A_j	Fourier coefficient
$b(x)$	width of ABM, m
D	bending rigidity, N m
E	Young's modulus, Pa
f	frequency, Hz
h	thickness of ABM, m
$k(x)$	wave number, m^{-1}
L_1	width of fluid channel, m
L_2	depth of fluid channel, m
L_3	length of ABM, m
p_f	pressure, Pa
w	displacement of ABM, m
$W(x)$	envelope function, m
(x, y, z)	Cartesian coordinates, m

Greek letters

$\eta(x, y)$	shape function for ABM's bending in y direction
ν	Poisson ratio
ρ_f	density of fluid, kg m^{-3}
ρ_m	density of PVDF, kg m^{-3}
$\phi_f(x, y, z, t)$	velocity potential, m^2/s
ω	angular frequency, rad/s

Subscripts

f	region of fluid channel f = l or u
j	mode number of Fourier coefficient
l	lower fluid channel
m	PVDF
u	upper fluid channel

of it, because of varying mechanical boundary conditions and the mechanical rigidity. Thus, when the eigen frequency at a local place match to that of acoustic wave, the place vibrates with relatively large amplitude due to the resonance. The vibration stimulates hair cells especially at the resonated place. As a result, the frequency of acoustic wave is recognized as the difference in tones.

To artificially realize the frequency selectivity, some microscaled devices have been reported. Tanaka et al. [5] and Xu et al. [6] developed acoustic sensors with the function of frequency selectivity by the use of resonance of cantilever arrays. Those sensors were evaluated in the atmospheric environment. Chen et al. [7] developed a beam array fixed on a trapezoidal channel and investigated the vibrating characteristics in the water. Despite the frequency selectivity of cantilevers or beams, their mechanical strength may not be enough for the implantation as the artificial cochleae for the long period. On the other hand, White and Grosh [8] developed a device made of polyimide membrane with Si_3N_4 beams. The demonstration for the frequency selectivity was conducted at the higher frequency range compared with the audible one. Wittbrodt et al. [9] also developed a device made of polyimide membrane with Al beams. They reported that the device possessed some similarities with the biological cochlea in terms of traveling waves, the frequency to place tonotopic organization, and the roll off beyond the characteristic place.

The acoustic sensor which is developed in this paper realizes both the frequency selectivity and the conversion of acoustic wave to the electric signal in the liquid environment without an external energy supply. The device is designed as a prototype model to test the basic concept of the acoustic sensor for the development of the self-contained implantable artificial cochlea. The device consists of a piezoelectric membrane fixed on a trapezoidal slit, where the membrane over the slit works as a detector. We name this trapezoidal membrane as an artificial basilar membrane (ABM). Discrete electrodes are fabricated on ABM by technologies of micro electromechanical systems (MEMS) to measure the electric signals generated in response to the externally applied acoustic waves. To model the liquid environment, the fluid channel which locates under ABM is filled with a silicone oil as a model of lymph fluid in the cochlea. The ABM's vibration is measured using a laser Doppler vibrometer (LDV) at the various frequencies in the range of 1.0–20 kHz. The electric output is measured through the electrodes using a preamplifier. To predict the performance of the present device, the oscillatory dynamics of ABM is theoretically analyzed based on the vibrating equation of a thin plate bending and equations for the fluid dynamics. The phenomenon of fluid-structure interaction is treated by coupling those basic equations. To treat the wave motion on trapezoidal ABM, the Wentzel–Kramers–Brillouin (WKB) asymptotic solution [10] is used under the assumption of the gradually varying wavelength. The comparison between the experimental and theoretical results makes clear the detailed mechanism underlying the frequency selectivity. In addition, discussions for the further development as an implantable artificial cochlea are described from the viewpoint of magnitude of electric signal and the device size.

2. Principles and experimental methods

2.1. Basic mechanism of frequency selectivity and electric signal generation

A schematic and a photograph of piezoelectric acoustic sensor developed here are shown in Fig. 1. The device comprises a polyvinylidine difluoride (PVDF) membrane (KUREHA, Japan) bonded on a stainless plate with a trapezoidal slit and discrete electrodes distributed along x axis. PVDF is a piezoelectric material which can convert mechanical stresses to electric signals. The trapezoidal slit is designed so that the membrane over it, i.e. ABM, can be easily vibrated by the acoustic wave. The width $b(x)$ of ABM is linearly varied in the ranges of 2.0–4.0 mm along x of 30 mm long. This shape is intended to mimic the passive basilar membrane, that is, the local resonant frequency (LRF) of ABM gradually changes due to the varying mechanical boundary conditions along x. LRF is expected to be decreased as x increases. Applying acoustic wave with a certain frequency to ABM, a local place vibrates with relatively large amplitude due to the resonance. Electric signals are generated by the piezoelectric effect with respect to the local stress in ABM. Thus, the electrode on the resonating place gives a relatively large electric output. This is the basic mechanism of frequency selectivity realized by the association of resonance of vibration and the discrete electrode array. The device is mounted on a substrate with a fluid channel, where the channel dimensions are 47 × 17 mm rectangle and 4 mm deep. To model an in vivo environment, the fluid channel is filled with silicone oil (Shin-Etsu Chemical, Japan). The density and the viscosity of silicone oil are 873 kg/m^3 and 1.75 × 10^{-3} Pa s, respectively, where those of lymph fluid in cochleae are typically reported as 1.0 × 10^3 kg/m^3 [11] and from 1.0 × 10^{-3} to 1.97 × 10^{-3} Pa s [12,13], respectively. Although the both sides of basilar membrane in vivo face to the lymph fluid, in this experiment, only the bottom side of ABM faces to the silicone oil for the stable optical measurement from the upper side. The effect of this simplification is discussed by the theoretical analysis in the later section. Furthermore, the size of this ABM is relatively large to be implanted into the human cochlea. However, the main purpose of this paper is to test the basic mechanism of proposed system in terms of acoustic/electric conversion and the frequency selectivity. The optimization and the miniaturization will be remained as a future work. The advantages of miniaturized ABM are again discussed in later section.

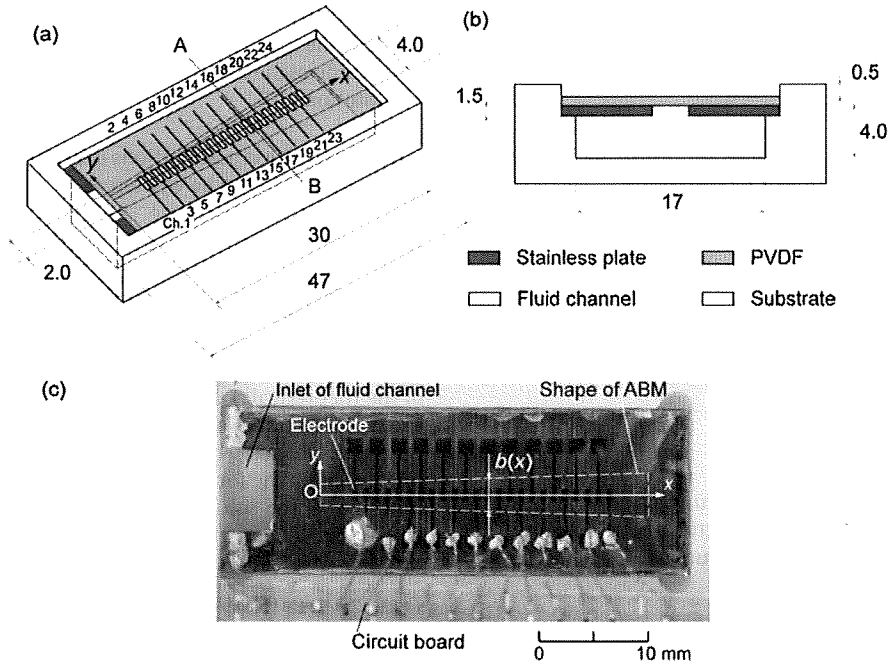

Fig. 1. Schematic and photograph of piezoelectric acoustic sensor; (a) 3D view, (b) cross sectional view at AB, and (c) photograph (Unit: mm).

2.2. Experimental setup

The electrode array with 24 elements made of an aluminum thin film is fabricated on an upper side of a 40 μm thick PVDF membrane based on a standard photolithography and an etching process. For convenience, the electrodes are named as Ch.1–Ch.24 as shown in Fig. 1(a). The each electrode of 0.50 × 1.0 mm rectangular shape is equally spaced 1.0 mm center to center, resulting in a gap of 0.50 mm between two adjacent electrodes. The ground electrode is prepared as a common one for all discrete electrodes on the lower side of ABM. The membrane is glued on the stainless plate to be the trapezoidal ABM. Since the electrodes of about 100 nm thick are extremely thinner than the PVDF of 40 μm, they may not strongly affect on the vibrating characteristics of ABM.

Fig. 2 shows a schematic of experimental setup. The sinusoidal acoustic wave is applied to the device from a speaker (FOSTEX, Japan) which is located 120 mm distant with 45° at a tilt. The speaker is previously calibrated to realize the constant sound pressure with the precision of ±0.1 dBSPL at various frequencies. The frequency is controlled by the function generator (NF, Japan) from 1.0 to 20 kHz which is in the range of audible frequency. The device on the substrate is set on a motorized stage which moves x and y directions for the measurement of spatial distribution of vibration amplitude. The velocity of ABM in z due to the vibration by the acoustic wave is measured by the LDV (Graphtec, Japan). The displacement, which is converted from the velocity data, is analyzed by an FFT to obtain the amplitude of vibration at the frequency of acoustic wave. At the same time, the piezoelectric output from the electrodes is measured in terms of voltage using a preamplifier and an oscilloscope.

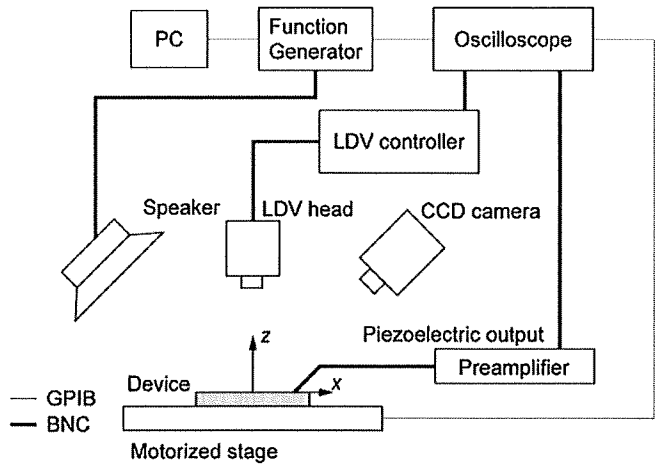

Fig. 2. Schematic of experimental setup for measurement of vibrating characteristics of ABM.

2.3. Oscillatory dynamics of artificial basilar membrane

Because the phenomena including the fluid-structure interaction are relatively complex, it is important for practical engineering to develop a theoretical model that effectively and easily predicts the vibrating characteristics of ABM. To obtain a mathematical solution, the following assumptions are made based on the experimental observations.

(1) The vibration of ABM is modeled as the bending vibration of a thin plate with small-amplitudes. The plain stress condition is valid, since the thickness h of ABM is small compared with the width or length.
(2) The fluid flow is assumed as incompressible, since $O(\omega^2 L^2/c^2)$ is 10^{-2}–10^{-6}, where the angular frequency ω is $O(10^3)$–$O(10^5)$, the characteristic length L is $O(10^{-3})$, and the sound velocity c is $O(10^3)$.
(3) The effects of gravity and viscosity of surrounding fluid are ignored.

The governing equation for the bending vibration of a plate with isotropic mechanical properties can be described as

$$\rho_m h \frac{\partial^2 w}{\partial t^2} + D\left[\frac{\partial^4 w}{\partial x^4} + 2\frac{\partial^4 w}{\partial x^2 \partial y^2} + \frac{\partial^4 w}{\partial y^4}\right] = p_0 \quad (1)$$

where D, p_0, w, and ρ_m are the bending rigidity, the pressure of acoustic wave, the displacement in z direction, and the density of ABM, respectively. The bending rigidity D is related to Young's modulus E as

$$D = \frac{Eh^3}{12(1-\nu^2)} \tag{2}$$

where ν is the Poisson ratio.

The basic equation for the fluid flow is the Laplace equation of velocity potential ϕ_f as

$$\frac{\partial^2\phi_f}{\partial x^2} + \frac{\partial^2\phi_f}{\partial y^2} + \frac{\partial^2\phi_f}{\partial z^2} = 0 \tag{3}$$

The velocity potential ϕ_f is related to the velocity components (u_x, u_y, u_z) as

$$u_x = \frac{\partial\phi_f}{\partial x}, \quad u_y = \frac{\partial\phi_f}{\partial y}, \quad u_z = \frac{\partial\phi_f}{\partial z} \tag{4}$$

respectively. The subscript f is u or l, where u and l indicate the fluid at the upper and lower sides of ABM, respectively. Furthermore, the velocity potential ϕ_f is related to the pressure as

$$\rho_f\frac{\partial\phi_f}{\partial t} = -p_f \tag{5}$$

where ρ_f is the density of fluid.

The governing equations are solved with the following boundary conditions. The normal velocities at the wall of fluid channel are written as

$$u_z = \frac{\partial\phi_l}{\partial z} = 0 \quad \text{at} \quad z = -L_2 \tag{6}$$

$$u_y = \frac{\partial\phi_l}{\partial y} = 0 \quad \text{at} \quad y = \pm\frac{L_1}{2} \tag{7}$$

where L_1 and L_2 are the width and the depth of fluid channel, respectively. The kinematic boundary condition at $z=0$ is written as

$$\frac{\partial w}{\partial t} = \frac{\partial\phi_f}{\partial z} \quad \text{at} \quad z = 0 \tag{8}$$

The thickness h of ABM is ignored in the analysis of fluid flow, since it is relatively small compared with the depth L_2 of fluid channel. The pressure p_0 is the pressure difference between the upper and lower sides of ABM and can be written as

$$p_0 = -\rho_l\frac{\partial\phi_l}{\partial t} + \rho_u\frac{\partial\phi_u}{\partial t} \quad \text{at} \quad z = 0 \tag{9}$$

Since ρ_l is extremely large compared with ρ_u in the present experiment, Eq. (9) is approximated as

$$p_0 \cong -\rho_l\frac{\partial\phi_l}{\partial t} \quad \text{at} \quad z = 0 \tag{10}$$

To obtain the oscillatory solution at the periodic steady state, following assumptions are made.

(4) A single mode $\eta(x, y)$ is used for the shape function of ABM's bending in y direction. $\eta(x, y)$ is determined based on the analytical solution of a vibrating beam with the first mode, the length of $b(x)$, and the fixed boundary conditions at $y = \pm b(x)/2$ as

$$\eta(x,y) = \begin{cases} c_1\cos\left(\frac{\beta}{b(x)}y\right) + c_2\cosh\left(\frac{\beta}{b(x)}y\right) & \text{at } -\frac{b(x)}{2} \le y \le \frac{b(x)}{2} \\ 0 \quad \text{at } -\frac{L_1}{2} \le y \le -\frac{b(x)}{2} \quad \text{and} \quad \frac{b(x)}{2} \le y \le \frac{L_1}{2} \end{cases} \tag{11}$$

where c_1, c_2, and β are constants of 0.8827, 0.1173 and 4.730, respectively. These constants are determined to make $\eta(x, y)$ satisfy the fixed boundary conditions at $y = \pm b(x)/2$.

(5) The wave is considered as a slowly varying wave in x direction. That is, the wave number $k(x)$ is slowly varying along x as $b(x)$, where $db(x)/dx \cong 0$ and $dk(x)/dx \cong 0$ are reasonable in the scale of a one wavelength. In this case, the waves can be treated as pseudo plane ones and can be described by the WKB asymptotic solution [10].

Based on these assumptions described above, the displacement $w(x, y, t)$ of ABM can be written as

$$w = W(x)\,\eta(x,y)\,e^{i\int_0^x k(\xi)d\xi}e^{-i\omega t} \tag{12}$$

where i and $W(x)$ are the imaginary number and the envelope function, respectively. $W(x)$ is also treated as a slowly varying function, that is $dW(x)/dx \cong 0$, since the effect of $dW(x)/dx$ on the dispersion relationship is trivial for linear problems [14]. The main purpose of the theoretical analysis is to predict the distribution of the local resonant frequency and to clarify the effect of the surrounding fluid on the resonance. Therefore, to simplify the mathematical development, only the forward wave is included in the analysis. On the other hand, the solution for Eq. (3) which satisfies the boundary conditions of Eqs. (6) and (7) is written as

$$\phi_l = \sum_{j=0}^{\infty} A_j\cosh\left[\zeta_j(z+L_2)\right]\cos\left(\frac{j\pi}{L_1}y\right)e^{i\int_0^x k(\xi)d\xi}e^{-i\omega t} \tag{13}$$

where A_j and ζ_j are the Fourier coefficient for jth mode and $[k^2(x)+(j\pi/L_1)^2]^{1/2}$, respectively. From Eqs. (8), (12) and (13), the following equation is obtained:

$$i\omega W(x)\eta(x,y) = -\sum_{j=0}^{\infty} A_j\zeta_j\sinh(\zeta_j L_2)\cos\left(\frac{j\pi}{L_1}y\right) \tag{14}$$

Using the orthogonality of cosine function, A_j is calculated as

$$A_j = -\frac{i\omega W(x)\int_{-b(x)/2}^{b(x)/2}\eta(x,y)\cos\left(j\pi y/L_1\right)dy}{\zeta_j\sinh\left(\zeta_j L_2\right)\int_{-L_1/2}^{L_1/2}\cos^2\left(j\pi y/L_1\right)dy} \tag{15}$$

Eqs. (10) and (12) are substituted into Eq. (1). Then, multiplying $\eta(x, y)$ to Eq. (1), and integrating from $-b(x)/2$ to $b(x)/2$ with respect to y, the following eikonal equation is obtained:

$$\begin{aligned} f(x,\omega) &= D\left[k^4(x)\int_{-b(x)/2}^{b(x)/2}\eta^2(x,y)dy - 2k^2(x)\right. \\ &\quad \left.\times\int_{-b(x)/2}^{b(x)/2}\eta(x,y)\,\partial^2\eta(x,y)/\partial y^2 dy + \left[\beta/b(x)\right]^4\int_{-b(x)/2}^{b(x)/2}\eta^2(x,y)dy\right] \\ &\quad -\omega^2\left[\rho_m h\int_{-b(x)/2}^{b(x)/2}\eta^2(x,y)dy + \rho_l\sum_{j=0}^{\infty}\frac{\left[\int_{-b(x)/2}^{b(x)/2}\eta(x,y)\cos\left(j\pi y/L_1\right)dy\right]^2}{\zeta_j\tanh\left(\zeta_j L_2\right)\int_{-L_1/2}^{L_1/2}\cos^2\left(j\pi y/L_1\right)dy}\right] \end{aligned} \tag{16}$$

Eq. (16) describes the dispersion relationship between $k(x)$ and ω at various x. The effect of surrounding fluid is found in the last term of Eq. (16). Since this term contributes to increase the effective mass for the vibration, the resonant frequency may be decreased by the surrounding fluid. From the average variation principle [14], it is known that the eikonal equation has the relationship with $W(x)$ as

$$W(x) = \frac{c}{\left(\frac{\partial f}{\partial k}\right)^{1/2}} \tag{17}$$

Table 1
Parameters for prediction.

Parameter	Symbol	Value
Width of ABM (m)	$b(x)$	$b(x)=0.002+0.002x/L_3$
Young's modulus of PVDF (Pa)	E	3×10^{9} [a]
Width of fluid channel (m)	L_1	0.017
Depth of fluid channel (m)	L_2	0.004
Length of ABM (m)	L_3	0.03
Poisson ratio of PVDF	ν	0.29 [a]
Density of PVDF (kg/m^3)	ρ_m	1780 [15]
Density of silicone oil (kg/m^3)	ρ_s	873 [b]
Density of air (kg/m^3)	ρ_a	1.2 [16]

[a] From technical report by KUREHA.
[b] From technical report by Shin-Etsu Chemical.

where c is a constant. Eq. (17) is the transport equation which describes the qualitative distribution of $W(x)$.

The parameters for the prediction are listed in Table 1. If the angular frequency ω is given as that of externally applied acoustic wave, only the wave number $k(x)$ is a variable to be solved in Eq. (16), where Eq. (16) is reduced to $f(k(x))=0$. At various ω, Eq. (16) is solved numerically by the Newton method. The iteration procedure is repeated until the residual becomes less than a specified tolerance of 10^{-6}. The term including summation is treated from $j=0$ to 30, which is adequate for the tolerance. The calculation is conducted for the two cases of filling the fluid channel with the air and of that with the liquid. The frequency is changed in the ranges of 3.5–14.0 kHz in the air environment and 0.7–3.6 kHz in the liquid environment, respectively. At those frequencies, Eq. (16) gives solutions and $W(x)$ has a peak on ABM.

Fig. 3 shows $W(x)$ which describes the qualitative amplitude distribution defined by Eq. (17). $W(x)$ in the air environment of Fig. 3(a) shows a clear peak at each frequency, where the peak indicates the resonance at the local place. Comparing $W(x)$ at different frequencies, it is found that the peak position shifts to smaller x as the frequency increases. It is also found that the peak value of $W(x)$ decreases as the frequency increases. Fig. 3(b) shows the $W(x)$ in the liquid environment. As same with the result in the air environment, the peak position shifts to smaller x as the frequency increases. However, compared with the results in the air environment, $W(x)$ in the liquid environment shows peaks at smaller frequencies. By comparing the results at 3.5 kHz in Fig. 3(a) and (b), the effect of the surrounding fluid on $W(x)$ can be discussed in detail. Although ABM is vibrated at the same frequency, it is found that the peak position in the liquid environment is shifted to smaller x and the form of $W(x)$ is moderated compared with those in the air environment. These results indicate that the stronger fluid-structure interaction due to the higher density decreases the resonant frequency and relaxes the resonance. Based on Eq. (16), the mechanism of decreasing the resonant frequency in the liquid environment is that the effective mass for the vibration is increased due to the much higher density of the liquid compared with that of the air. The reason for the moderated resonance is discussed later.

Fig. 4(a) shows the distributions of $k(x)$ in the air environment at 3.5, 6.0, 9.0, and 12.0 kHz. In Fig. 4(a), it is found that $k(x)$ in the air environment increases with x. There is a certain position of x_{inc} where $k(x)$ rapidly increases. x_{inc} is mathematically defined as the position where $k(x)$ gives the largest gradient. At larger x than x_{inc}, $O(k(x))$ is 10^2–10^3 m^{-1} and the wavelength is 63–6.3 mm. At smaller x than x_{inc}, $k(x)$ is very small which corresponds to the extremely long wavelength. Comparing the results at different frequencies, it is found that x_{inc} becomes smaller at the higher frequency. It is also found that x_{inc} is close to the peak position of $W(x)$ in Fig. 3(a). Since the result is obtained by the analysis based on the WKB solution, the wavelength should be short enough to treat $b(x)$ as a slowly varying function. Furthermore, $k(x)$ should be gradually changed by x. Thus, the precision of result should be relatively bad around x_{inc} and at smaller x than x_{inc}. Fig. 4(b) shows the $k(x)$ distributions in the liquid environment at 1.0, 2.0, 3.0, and 3.5 kHz. $k(x)$ in the liquid environment gradually increases with x compared with that in the air environment. Although the resonant frequencies are different between in the air and in the liquid envi-

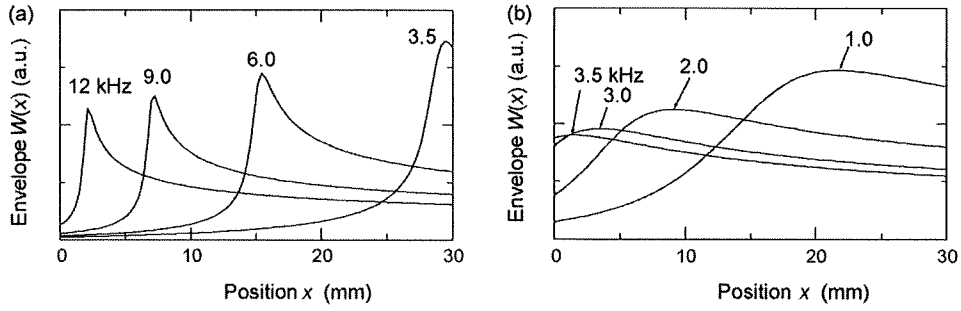

Fig. 3. Theoretical results of envelope function $W(x)$ in (a) air and in (b) liquid environments for various frequencies.

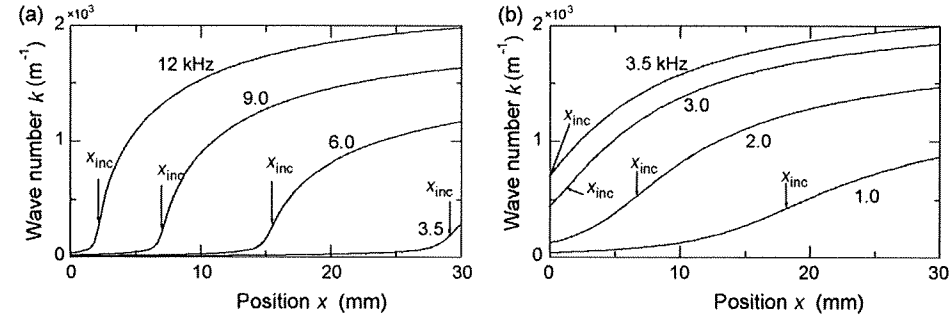

Fig. 4. Theoretical results of wave number $k(x)$ in (a) air and in (b) liquid environments for various frequencies.

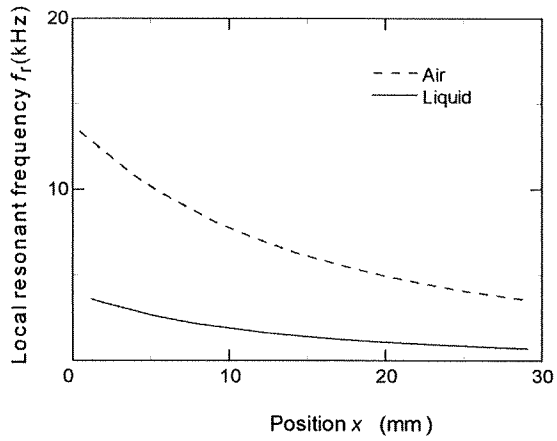

Fig. 5. Theoretical results of local resonant frequencies in air and in liquid environments.

ronments, the orders of $k(x)$ around x_{inc} and at larger x than x_{inc} are similar to the results in the air environment. From this result, it can be said that the resonance is governed by the wavelength which is strongly related to the geometry of ABM. x_{inc} is closely connected with the peak position of $W(x)$ shown in Fig. 3(b). Furthermore, the reason for the moderated resonance in the liquid environment can be explained by comparing Fig. 4(a) and (b). Since $k(x)$ in the air environment rapidly changes around the resonance place as shown in Fig. 4(a), the evolution of $W(x)$ also does. It is owing to the fact that the resonance condition is governed by the wavelength. On the contrary, since $k(x)$ in the liquid environment gradually changes around the resonance place as shown in Fig. 4(b), the peak of $W(x)$ becomes to be moderated.

Fig. 5 shows the relationship between the resonant frequency f_r and x. Both f_r in the air and in the liquid environments decrease as x increases and f_r in the liquid environment is lower than that in the air environment due to the increase of effective mass. Although the auditory frequency is widely ranged from 20×10^{-3} to 20 kHz, the device can cover only the part of it. It works at the frequencies over the ranges of 3.5–14 kHz in the air environment and 0.7–3.6 kHz in the liquid environment, respectively. For the clinical application, the device should be optimized to realize the frequency selectivity in the required frequency range for a daily conversation. Furthermore, distribution of f_r should be fitted to that in the biological system from the viewpoint of natural hearing. To solve these problems, the geometrical optimizations of ABM can be effectively carried out in our future work based on the theoretical analysis developed here.

The theoretical analysis is carried out based on the experimental condition, where only the bottom side of ABM faces to the liquid. In case of ABM facing to the liquid at both sides, the difference is found in the last term of Eq. (16) which includes the effect of surrounding fluid. In case of the same fluid channel is placed on the upper side of ABM and is filled with the same liquid, the last term is double of that in Eq. (16). Consequently, the larger effect of surrounding fluid is induced, that is, the further decrease of resonant frequency is found due to the increase of effective mass for the vibration, where the figure is omitted.

Furthermore, the theoretical analysis is carried out based on the assumption of the small amplitude. The basic equations are solved by WKB treatment which cannot quantitatively predict the vibrating amplitude. Therefore, it is difficult to precisely estimate the piezoelectric output which is determined by the strain in the membrane. The investigation on the piezoelectric output can be made by the numerical analysis based on the finite element method, which is our future research.

3. Results and discussion

3.1. Performance test in air environment

The basic vibrating characteristics of ABM in the air environment are investigated as a preliminary experiment. This experiment is conducted without filling the fluid channel with the silicone oil. The amplitude distributions of vibration are measured by applying acoustic waves of 75 dBSPL. The frequency is controlled over the range of 1.0–20.0 kHz, which covers the part of human's audible frequency. The amplitude of vibration becomes relatively small at the frequencies both lower than 3.0 kHz and higher than 18.0 kHz. It may be owing to that ABM is designed to have LRF for the first mode over the range of 3.5–14.0 kHz in the air environment. Fig. 6(a)–(d) show the amplitude distribution at f = 4.0, 6.0, 9.0, and 12.0 kHz, respectively. The amplitude distribution clearly shows dependence on the frequency. The place with maximum amplitude, where ABM is locally resonating, shifts to the smaller x as the frequency increases. This relationship between the position of resonating place and the frequency successfully has similarities with that of biological basilar membranes. Furthermore, in Fig. 6(c) and (d), it is found that there are several extrema indicated by arrows at the larger x than that of resonating place. These may be induced by the standing wave due to the traveling waves to positive and negative directions of x. The reason why the standing wave is not observed at the smaller x than that of resonating place is that the wavelength is relatively long at those positions. This is confirmed by the theoretical result of relatively small $k(x)$ as shown in Fig. 4(a). In the biological cochlea, the acoustic wave travels from the basal to the apex. However, in our experiment, it is applied to the entire ABM from the air. As a result, the relatively large effects of the standing waves are induced in our experiment due to the small damping effects from the surrounding fluid.

Fig. 7(a)–(c) show the frequency dependences of vibration and the piezoelectric output at Ch. 6, Ch. 12 and Ch. 18, respectively. The amplitudes of vibration and the piezoelectric output are plotted by a solid line and by a broken line, respectively. It seems that each electrode has a specific frequency where the electrode gives

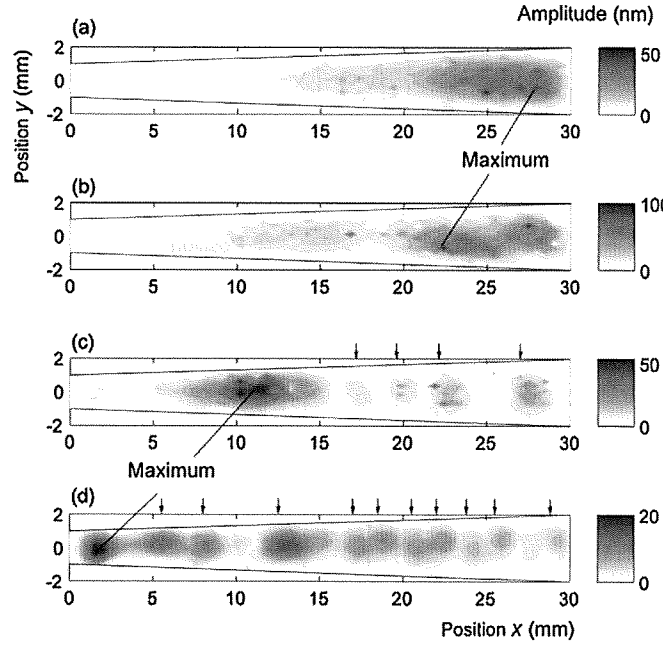

Fig. 6. Experimental results of contour maps of vibration amplitude at (a) f = 4.0 kHz, (b) 6.0 kHz, (c) 9.0 kHz, and (d) 12.0 kHz in air.

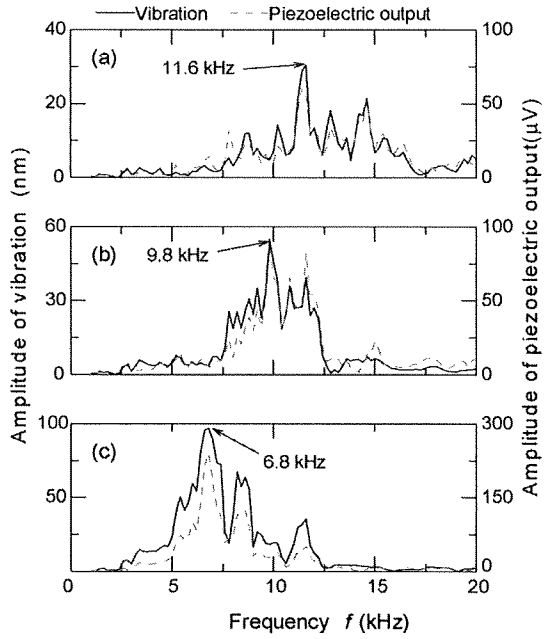

Fig. 7. Experimental results of vibration amplitude and piezoelectric output from (a) Ch. 6, (b) Ch. 12 and (c) Ch. 18 at various frequencies in air.

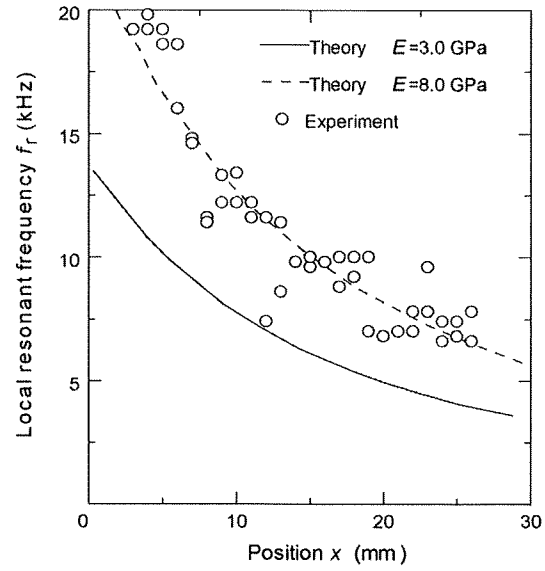

Fig. 8. Comparison of theoretically and experimentally obtained results of local resonant frequency f_r in air.

relatively large outputs. The specific frequency is defined as LRF of electrode. LRF decreases as the channel number increases, i.e., as the position x increases. Extremal amplitudes at other frequencies of LRF may indicate the effect of standing waves. That is, in case of the electrode locates on the antinode of standing wave, the amplitude from the electrode increases. On the other hand, in case of the electrode locates on the node, the amplitude decreases. As reported in Refs. [7,8,17], pretension in the membrane may be a main reason for the standing wave which results in the multiple-peaks as shown in Fig. 7. However, it is difficult to precisely control the pretension in our fabrication process. Therefore, the mechanism of this result remained to be solved in this study. The frequency dependences of vibration and the piezoelectric output are qualitatively similar to each other. The reason of their similarity can be explained as follows. Since ABM is relatively narrow in y direction compared with that in the x direction, the vibration is mainly effected by the boundary conditions at $y = \pm b(x)/2$. As the result of that, the piezoelectric output is dominated by the ABM's local structural strain in y direction. Furthermore, the piezoelectric constant in y direction is larger than that in x direction. This may make the strong dependence of piezoelectric output on the strain in y direction.

Fig. 8 shows the relationship between LRF f_r and position x. Circles are LRF which are determined by the vibration and the piezoelectric output. LRF decreases from 19.8 to 6.6 kHz as x increases. This experimental LRF is in qualitative agreement with the theoretical prediction of Eq. (16) which is drawn by the solid line. In the quantitative comparison, however, almost all experimental results are slightly higher than the predictions. One of possible reasons is the underestimation of E. Since E from literatures widely distributes as 3.0–11.0 GPa [18,19], we used a reference value of 3.0 GPa for the prediction. If we use higher value of 8.0 GPa, the precision is improved as shown by the broken line in Fig. 8.

Fig. 9(a) shows the relationship between the external sound pressure and the amplitude of vibration in ABM. This investigation is conducted at LRF of each electrode. To show the results over the range of 60–90 dBSPL, those are drawn in the log-dBSPL plot. From the gradient of results, it is found that the amplitude of vibration at LRF linearly increases with the sound pressure. The amplitude increases with the channel number, that is, with ABM's width. Fig. 9(b) shows the relationship between the sound pressure and the amplitude of piezoelectric output. The amplitude of piezoelectric output also shows the linear relationship with the sound pressure. These results suggest that the device can detect not only the frequency of acoustic wave but also the magnitude of it.

3.2. Performance test in liquid environment

The performance of device in the liquid environment is investigated by filling the fluid channel with the silicone oil with the

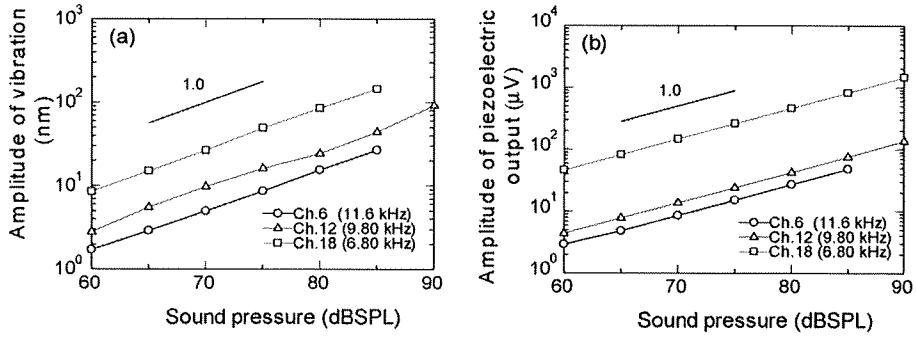

Fig. 9. Experimental results in effect of sound pressure on amplitudes (a) of vibration and (b) of piezoelectric output in air.

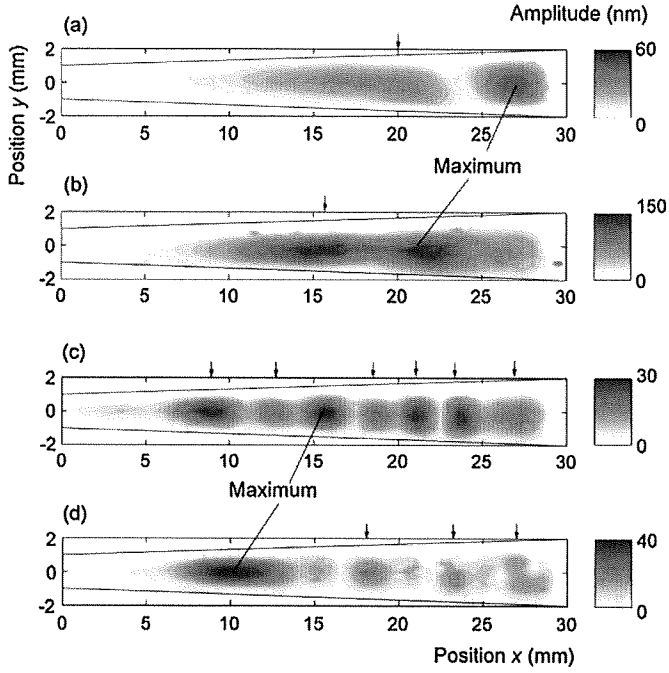

Fig. 10. Experimental results of contour maps of vibration amplitude at (a) f = 1.5 kHz, (b) 2.0 kHz, (c) 3.0 kHz and (d) 4.0 kHz in silicone oil of 1.75×10^{-3} Pa s.

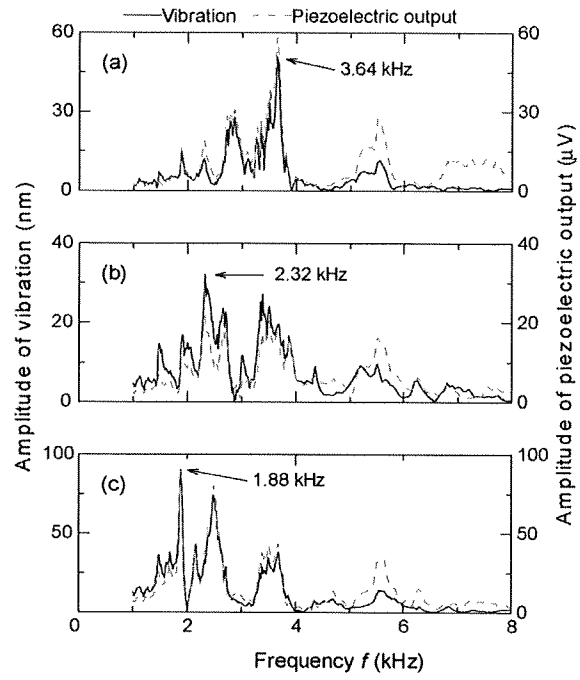

Fig. 11. Experimental results of vibration amplitude and piezoelectric output from (a) Ch. 6, (b) Ch. 12 and (c) Ch. 18 at various frequencies in silicone oil of 1.75×10^{-3} Pa s.

viscosity of 1.75×10^{-3} Pa s. This investigation is intended to test the applicability of device for implanting into the cochlea. Since the outputs from ABM are relatively small compared with that in the air environment, the sound pressure is increased to be 85 dBSPL for this experiment. This decrease of outputs in the silicone oil may be caused by energy dissipation in liquid environment due to the viscosity and the stronger fluid-structure interaction of ABM due to the density, however, the detailed mechanism has not been clarified. Fig. 10 shows the contour maps of amplitude distribution at (a)f = 1.5 kHz, (b)2.0 kHz, (c)3.0 kHz and (d) 4.0 kHz, respectively. The qualitative frequency dependence of vibration is similar to that in the air environment. That is, the location with the maximum amplitude is shifted to the smaller x as the frequency increases. However, the frequency ranges where ABM shows peak amplitude in the silicone oil are lower than that in the air environment. Comparing Fig. 6(a) and Fig. 10(d), the effect of surrounding fluid can be discussed in detail. In spite of driving the device at the same frequency of 4.0 kHz, these results clearly show the different vibration behavior. It is found that the maximum amplitude is found at the smaller x in the silicone oil compared with that in the air environment. This difference may be caused by the fluid-structure interaction as discussed in the earlier section. That is, compared with the result in the air environment, the effective mass for the vibration is increased in the silicone oil. As a result, the place with maximum amplitude is shifted to the smaller x in the silicone oil at the same frequency. Furthermore, the effects of standing wave in the silicone oil which are indicated by arrows seem relatively large compared with that in the air environment. This fact is predicted by the theoretical analysis that the resonance is relaxed due to the surrounding liquid as shown in Fig. 3.

Fig. 11 shows the frequency dependences of vibration and piezoelectric output, where they are indicated by a solid line and the broken one, respectively. As same with those in the air environment, the two amplitudes show the similar tendency to each other. The amplitudes have peaks at each specific frequency which is also described as LRF for convenience. LRF of Ch. 6, Ch. 12, and Ch. 18 are obtained as 3.64, 2.32, and 1.88 kHz, respectively. From Fig. 11, it is confirmed that the ABM's frequency selectivity is successfully realized even in the liquid environment. However, comparing Figs. 7 and 11, the peak height at the LRF becomes low, i.e., the selectivity seems worse than that in the air environment. This result qualitatively agrees with the theoretical result that the peak is relaxed in the liquid environment as shown in Fig. 3. In order to dramatically improve the frequency selectivity, it is expected that the sensor including the active feedback control which mimics the biological cochlea should be developed in future.

Fig. 12 shows the relationship between f_r and x in the silicone oil. From Fig. 12, it is found that the LRF decreases from 4.9 to 1.4 kHz as x increases, where the range is lower than that in the air environment. The experimentally obtained LRF is compared

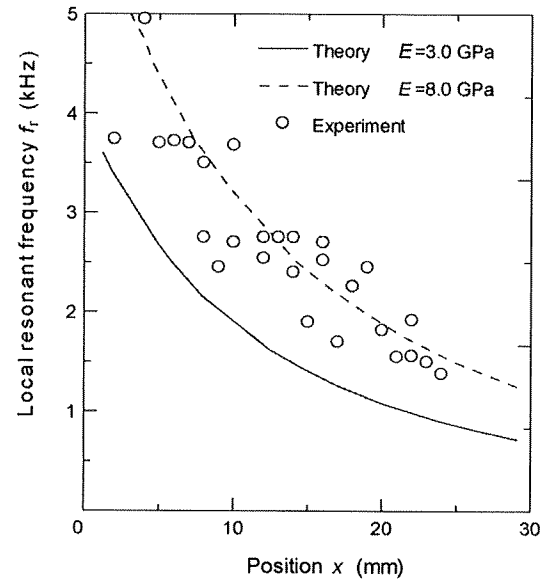

Fig. 12. Comparison of theoretically and experimentally obtained results of local resonant frequency f_r in silicon oil of 1.75×10^{-3} Pa s.

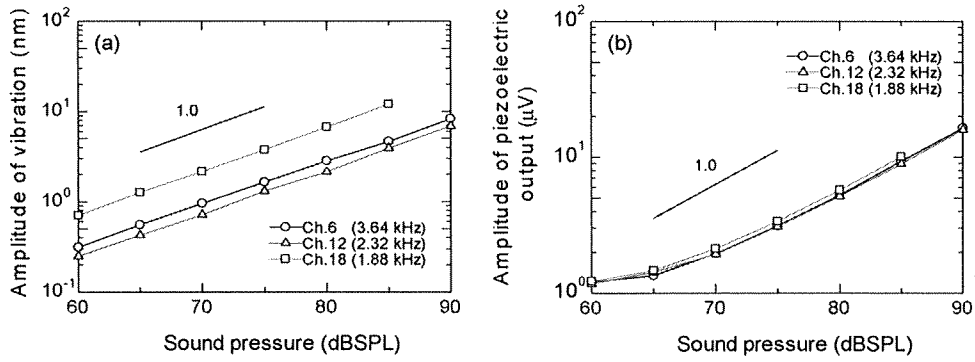

Fig. 13. Experimental results in effect of sound pressure on amplitudes (a) of vibration and (b) of piezoelectric output in silicone oil of 1.75×10^{-3} Pa s.

with the theoretically obtained one in Fig. 12. The predicted LRF of $E = 8.0$ GPa which is drawn by the broken line reasonably agrees with the experimentally obtained ones. From this agreement, it can be said that the theoretical analysis well reproduces the effect of the fluid-structure interaction on LRF. Since the theoretical analysis is carried out with inviscid fluid model, it can also be said that the decrease of LRF in the liquid environment is governed by the increase of effective mass for the vibration under the condition of constant sound pressure.

Fig. 13(a) shows the relationships between the sound pressure and the amplitudes of vibration. The amplitude of vibration linearly increases with the sound pressure. However, the amplitude of piezoelectric output shown in Fig. 13 (b) seems to be nonlinear especially at the low sound pressure level of 60–70 dBSPL. It may be due to the viscosity of liquid, however, it is difficult to confirm the reason for the nonlinear relationship due to the lack of the basic knowledge, where it is in our future work. As shown in Fig. 13(b), the amplitude of piezoelectric output is about 16 μV at 90 dBSPL in the silicone oil. The acoustic wave of 90 dBSPL is relatively loud for the normal hearing. Even applying such a high sound pressure, the developed device can generate several tens of μV at most. To effectively stimulate nerve cells [20], the electric output should be amplified. One of the methods for the amplification is to use equipment such as a hearing aid, where it amplifies the sound pressure. Another solution is the downsizing of device using a fully micromachining process, since the thinner membrane can generate the larger voltage. That is, the piezoelectric voltage V_p is proportional to the stress σ and the square of thickness h as $V_p \propto \sigma h^2$. On the other hand, the stress σ of ABM is inversely proportional to the cube of thickness as $\sigma \propto h^{-3}$. Consequently, the voltage is inversely proportional to the thickness as $V_p \propto h^{-1}$. The reduction of thickness can be easily realized by means of microfabrication and the thin films technologies. Thus, the implantable device will be developed based on those technologies in our future work.

3.3. Effect of viscosity on frequency selectivity

Fig. 14 shows the contour maps of amplitude distribution using the higher viscous silicone oil of 1.75×10^{-2} Pa s at (a)$f = 1.5$ kHz, (b)2.0 kHz, (c)3.0 kHz and (d) 4.0 kHz, respectively. The viscosity of the silicone oil is ten times higher than that in the previous section. The positions of maximum amplitude are $x = 28.0$, 24.0, 20.5, and 10.5 mm for $f = 1.5$, 2.0, 3.0, and 4.0 kHz, respectively as shown in Fig. 14. On the other hand, those are $x = 27.0$, 21.0, 16.0, and 10.0 mm in the results of 1.75×10^{-3} Pa s as shown in Fig. 10. From this result, it can be said that the effect of viscosity on the position of the resonating place seems small. It is also found that the local maximum amplitudes due to the standing wave are relatively small in Fig. 14 compared with those in Fig. 10. That is

Table 2
Ratio a_1/a_2 of height between the highest peak and the secondary highest one.

Frequency f (Hz)	Ratio at 1.75×10^{-3} Pa s a_1/a_2	Ratio at 1.75×10^{-2} Pa s a_1/a_2
1.5	1.52	1.69
2.0	1.03	1.56
3.0	1.08	1.96
4.0	1.89	2.08

quantitatively confirmed by the ratio a_1/a_2 which is the ratio of amplitudes between the highest peak a_1 and the secondary highest peak a_2 in Table 2. Comparing the results between 1.75×10^{-3} Pa s and 1.75×10^{-2} Pa s, it is found that the highest peak is significant in the higher viscous silicone oil. This may be caused because the wave is damped more rapidly in the higher viscous one. From the viewpoint of application, this result indicates that the effect of viscosity may contribute to improve the frequency selectivity. It is also possible to discuss the effect of viscosity by comparing the result between in the air and in the liquid environments. However, there are two different types of fluid-structure interactions of the increase in the effective mass and the viscous damping between

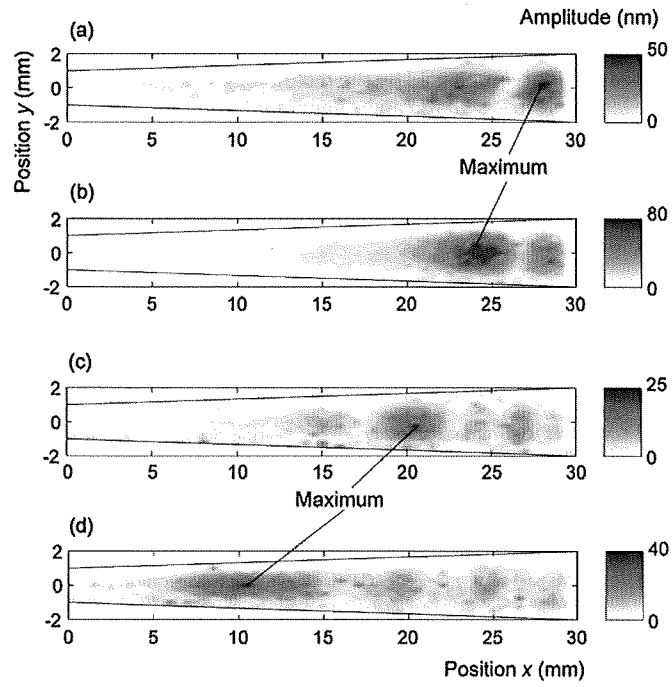

Fig. 14. Experimental results of contour maps of vibration amplitude at (a) $f = 1.5$ kHz, (b) 2.0 kHz, (c) 3.0 kHz and (d) 4.0 kHz in silicone oil of 1.75×10^{-2} Pa s.

those conditions. Since they contribute to the frequency selectivity oppositely, it is difficult to discuss separately. The development of theoretical analysis using full Navier-Stokes equation should be made in future research.

4. Concluding remarks

In this paper, we reported a novel piezoelectric artificial cochlea which worked as a sensor with the acoustic/electric conversion and with the frequency selectivity based on MEMS technology. The basic performances of prototype device both in the air and in the liquid environments were investigated experimentally and theoretically.

The vibrating characteristics of trapezoidal ABM were measured by applying acoustic waves at a certain frequency. The location with the maximum amplitude was shifted toward narrower area of trapezoidal ABM as the frequency increased. This phenomenon indicated that the developed device successfully realized the frequency selectivity.

The frequency dependences of vibration and piezoelectric output were investigated both in the air and in the silicone oil of 1.75×10^{-3} Pa s. The resonant frequencies were determined to be over the ranges of 6.6–19.8 kHz in the air and 1.4–4.9 kHz in the silicone oil, respectively. The decrease in the resonant frequency due to the silicone oil must be the effect of fluid-structure interaction, that is, the interaction between the acoustic wave in the fluid and the membrane vibration. The interaction contributed to increase the effective mass for the vibration. This consideration was confirmed by the reasonable agreement between the experiment and the theory in terms of local resonant frequency.

The viscous effect of surrounding fluid on the vibration was explored using the higher viscous silicone oil of 1.75×10^{-2} Pa s. The effect on the resonating place seemed to be small between 1.75×10^{-3} and 1.75×10^{-2} Pa s. However, it was found that the higher viscous liquid suppressed the standing wave and improved the frequency selectivity.

To develop the fully implantable device in our future work, the amplification of voltage may be required to effectively stimulate nerve cells. Furthermore, the present device is relatively large for the implantation into a cochlea. These problems can be solved by the use of microfabrication and thin films technologies. The miniaturization is accomplished by the technology straightforward. And the larger electric signals can be generated using the thinner ABM, since the voltage is expected to be inversed proportional to the thickness. As a matter of course, these further developments must be conducted considering the frequency dependence. Thus, the theoretical approach which is described here is useful to design it in our future work.

References

[1] F.G. Zeng, Trends in cochlear implants, Trends Amplification 8 (1) (2004) T1–T34.
[2] S.B. Waltzman, Cochlear implants: current status, Expert Rev. Med. Dev. 3 (5) (2006) 647–655.
[3] G.V. Békésy, Current status of theories of hearing, Science 123 (3201) (1956) 779–783.
[4] G.V. Békésy, Hearing theories and complex sounds, J. Acoust. Soc. Am. 35 (4) (1963) 588–601.
[5] K. Tanaka, M. Abe, S. Ando, A novel mechanical cochlea "fishbone" with dual sensor/actuator characteristics, IEEE ASME Trans. Mechatron. 3 (2) (1998) 98–105.
[6] T. Xu, M. Bachman, F.G. Zeng, G.P. Li, Polymeric micro-cantilever array for auditory front-end processing, Sens. Actuators A Phys. 114 (2–3) (2004) 176–182.
[7] F. Chen, H.I. Cohen, T.G. Bifano, J. Castle, J. Fortin, C. Kapusta, D.C. Mountain, A. Zosuls, A.E. Hubbard, A hydromechanical biomimetic cochlea: experiments and models, J. Acoust. Soc. Am. 119 (1) (2006) 394–405.
[8] R.D. White, K. Grosh, Microengineered hydromechanical cochlear model, Proc. Natl. Acad. Sci. U.S.A. 102 (5) (2005) 1296–1301.
[9] M.J. Wittbrodt, C.R. Steele, S. Puria, Developing a physical model of the human cochlea using microfabrication methods, Audiol. Neurootol. 11 (2) (2006) 104–112.
[10] C.R. Steele, L.A. Taber, Comparison of WKB calculations and experimental results for three-dimensional cochlear models, J. Acoust. Soc. Am. 65 (4) (1979) 1007–1018.
[11] J.D. Bronzino, The Biomedical Engineering Handbook, CRC Press, 1995.
[12] G. Zhou, L. Bintz, D.Z. Anderson, A life-sized physical model of the human cochlea with optical holographic readout, J. Acoust. Soc. Am. 93 (3) (1993) 1516–1523.
[13] J.H. ten Kate, J.W. Kuiper, The viscosity of the pike's endolymph, J. Exp. Biol. 53 (2) (1970) 495–500.
[14] G.B. Whitham, Linear and Nonlinear Waves, Wiley-Interscience, 1974.
[15] M. Chanda, S.K. Roy, Plastic Technology Handbook, CRC press, 2006, pp. 5–52.
[16] National Astronomical Observatory of Japan, Chronological scientific tables (2009), Maruzen.
[17] K.M. Lim, A.M. Fitzgerald, C.R. Steele, Building a physical cochlear model on a silicon chip, in: H. Wada, T. Takasaka, K. Ikeda, K. Ohyama, T. Koike (Eds.), Recent Developments in Auditory Mechanics, World scientific, 1999, pp. 223–229.
[18] J. Sirohi, I. Chopra, Fundamental understanding of piezoelectric strain sensors, J. Intell. Mater. Syst. Struct. 11 (4) (2000) 246–257.
[19] H. Ohigashi, Electromechanical properties of polarized polyvinylidene fluoride films as studied by the piezoelectric resonance method, J. Appl. Phys. 47 (3) (1976) 949–955.
[20] Y. Jimbo, T. Tateno, H.P.C. Robinson, Simultaneous induction of pathway-specific potentiation and depression in networks of cortical neurons, Biophys. J. 76 (2) (1999) 670–678.

Biographies

Hirofumi Shintaku received B.S., M.S., and Ph.D. degrees from Department of Mechanical Engineering, Kyoto University, Japan, in 2002, 2004, and 2006, respectively. Since 2006, he has been an Assistant Professor in Department of Mechanical Science and Bioengineering, Graduate School of Engineering Science, Osaka University, Japan. His current research area is fluid dynamics in the micro and nano meter scales.

Takayuki Nakagawa received M.D. and Ph.D. from Medical School, Osaka City University, Japan in 1989 and 1995, respectively. From 1995 to 2001, he was a Department Director in Department of Otolaryngology, Yodogawa Christian's Hospital, Osaka, Japan. From 2001 to 2008, he was an Assistant Professor in Department of Medicine, Graduate School of Medicine, Kyoto University, Japan. Since 2008, he has been a Lecturer in Kyoto University.

Dai Kitagawa received B.S. degree from Department of Mechanical Science and Bioengineering, Osaka University, Japan, in 2007. Since 2007, he has been a master course student in Department of Mechanical Science and Bioengineering, Graduate School of Engineering Science, Osaka University.

Harto Tanujaya received B.S. and M.S. degree from Tarumanagara University, Indonesia and University of Indonesia in 1996 and 1999, respectively. Since 2000, he has been a Lecturer at Department of Mechanical Engineering, Faculty of Engineering, Tarumanagara University. Furthermore, since 2007, he has been a Ph.D. course student in the Department of Mechanical Science and Bioengineering, Graduate School of Engineering Science, Osaka University, Japan.

Satoyuki Kawano received B.S., M.S., and Ph.D. degrees in Mechanical Engineering from Tohoku University, Japan in 1987, 1989 and 1992, respectively. Following graduation he was a Postdoctoral Fellow of the Japan Society for the Promotion of Science in 1992. He was appointed as a Research Assistant in 1993 and as an Associate Professor in 1996 at Tohoku University. In the year of 2005, he was appointed as a Professor at Osaka University where he served as the Chair of the Division of Mechanical Engineering of the Graduate School of Engineering Science from 2006 to 2009. His current research interest is molecular fluid dynamics including interfacial phenomena, plasmas, blood cells and biomacromolecules.

Juichi Ito received M.D. and Ph.D. from Department of Medicine, Kyoto University, Japan, in 1975 and 1983, respectively. From 1983 to 1985, he was an Assistant Professor in Neurology, University of California, Los Angeles. From 1985 to 1990, he was a Lecturer in Department of Otolaryngology Head and Neck Surgery Kyoto University Hospital. From 1990 to 2000, he was a Chief in Otorhinolaryngology and Broncho-Esophagology, Otsu Red-Cross Hospital. Since 2000, he has been a Professor and Chairman of Department of Otolaryngology Head and Neck Surgery, Graduate School of Medicine, Kyoto University.

The Laryngoscope

Transplantation of Bone Marrow-Derived Neurospheres Into Guinea Pig Cochlea

Hideaki Ogita, MD; Takayuki Nakagawa, MD, PhD; Tatsunori Sakamoto, MD, PhD; Takatoshi Inaoka, MD; Juichi Ito, MD, PhD

Objectives/Hypothesis. To investigate the potential of neurally induced bone marrow stromal cells (BMSCs) as transplants for replacement of spiral ganglion neurons.

Methods. BMSCs were harvested from the femurs and tibias of adult guinea pigs. BMSCs were cultured with neural induction media and formed spheres. The capacity of BMSC-derived spheres for neural differentiation was examined by immunocytochemistry in vitro. BMSC-derived spheres were injected into the modiolus of the intact cochleae or those locally damaged by ouabain, followed by histological and functional analyses.

Results. In vitro analysis revealed a high capacity of BMSC-derived spheres for neural differentiation. After transplantation into the cochlear modiolus, the survival and neural differentiation of BMSC-derived spheres was observed in both the intact and damaged cochleae. In intact cochleae, transplants settled in various portions of the cochlea, including the cochlear modiolus, whereas in damaged cochleae, transplants were predominantly observed in the internal auditory meatus. Transplantation of BMSC-derived spheres resulted in no functional recovery of the cochlea or protection of host spiral ganglion neurons.

Conclusions. The present findings indicate that BMSC-derived spheres can be a source for replacement of spiral ganglion neurons, although further manipulations are required for functional recovery.

Key Words: Allograft, cell therapy, cochlea, neurosphere, spiral ganglion neuron, regeneration.

***Laryngoscope*, 000:000–000, 2009**

INTRODUCTION

Treatment options for sensorineural hearing loss are currently limited to cochlear implants and hearing aids. Hence, there is a requirement for alternative means of biological therapy, including cell-based therapy. Indeed, recent studies have indicated that cell-based therapy could be utilized as a therapeutic option for inner ear disorders.[1–3] Spiral ganglion neurons (SGNs), primary auditory neurons, are located in the modiolus of the cochlea and transmit sound stimulation to the central auditory system. The loss of SGNs, therefore, compromises auditory function. In addition, SGN loss also reduces the effectiveness of cochlear implants, which can improve impaired hearing by stimulating SGNs. SGNs are, therefore, a primary target for cell transplantation in the auditory system.

Bone marrow stromal cells (BMSCs) are a heterogeneous population of stem/progenitor cells with pluripotent capacity to differentiate toward a neuronal phenotype,[4,5] and consequently the possible use of BMSCs for the treatment of neurological diseases has acquired enormous importance. BMSCs have great potential as therapeutic agents, because they are easy to isolate and expand. Previously, the potential of BMSC transplantation for the treatment of inner ear disorders has been investigated.[6–9] These previous studies have demonstrated that undifferentiated BMSCs are able to settle in the cochlea and have a high capacity for migration. However, limited numbers of transplants differentiated into neurons after transplantation into the intact or damaged cochlea,[6–8] which indicates that neural induction of BMSCs before transplantation is required for SGN replacement by BMSC transplantation.

The aim of this study was to elucidate the neural expression profile of neurally induced BMSCs of guinea pigs and their ability to retain neural differentiation potential when transplanted into the intact or damaged cochleae of guinea pigs. In addition, we examined the capacity of neurally induced BMSCs for functional and histological replacement of SGNs.

MATERIALS AND METHODS

Experimental Animals

A total of 18 Hartley-strain guinea pigs were purchased from Japan SLC Inc. (Hamamatsu, Japan). The Animal

From the Department of Otolaryngology–Head and Neck Surgery, Graduate School of Medicine, Kyoto University, Kyoto, Japan.

Editor's Note: This Manuscript was accepted for publication October 13, 2009.

This study was supported by a Grant-in-Aid for Research on Sensory and Communicative Disorders from the Japanese Ministry of Health, Labor and Welfare.

Send correspondence to Takayuki Nakagawa, MD, PhD, Department of Otolaryngology–Head and Neck Surgery, Graduate School of Medicine, Kyoto University, Kawaharacho 54, Shogoin, Sakyo-ku, 606-8507 Kyoto, Japan. E-mail: tnakagawa@ent.kuhp.kyoto-u.ac.jp

DOI: 10.1002/lary.20776

Research Committee of the Graduate School of Medicine, Kyoto University, Kyoto, Japan, approved all of the experimental protocols. Animal care was carried out under the supervision of the Institute of Laboratory Animals of the Graduate School of Medicine, Kyoto University. All of the experimental procedures were performed in accordance with the National Institutes of Health Guidelines for the Care and Use of Laboratory Animals.

BMSCs

Bone marrow was isolated from the femurs and tibias of 6- to 8-week-old guinea pigs (n = 4, Japan SLC Inc.). Under general anesthesia with midazolam (8 mg/kg, intramuscular injection) and xylazine (8 mg/kg, intramuscular injection), the epiphyses of the femurs and tibias were removed, and the marrow was flushed out into a 100-mm culture dish. The isolated bone marrow, composed of hematopoietic and stromal cells, was maintained in Dulbecco's Modified Eagle's Medium (DMEM) (Invitrogen, Gaithersburg, MD) supplemented with 10% fetal bovine serum (Thermo Trace Ltd., Noble Park, Victoria, Australia) and 1% antibiotic-antimycotic (Invitrogen) at 37°C with 5% CO_2. The medium was changed twice weekly until the cells were 80% confluent. Nonadherent cells were removed during the medium-change procedure. The BMSCs were passaged three to five times before use. BMSCs at this stage were defined as undifferentiated.

Neural Induction of BMSCs

For neural induction, cultured BMSCs were enzymatically detached from culture dishes. The BMSCs were plated into 100-mm culture dishes at a density of 2×10^6 cells/well, and cultured in serum-free DMEM/F-12 medium (Invitrogen) supplemented with B27 (Invitrogen), 20 ng/mL of basic fibroblast growth factor (bFGF, Invitrogen), and 20 ng/mL of epidermal growth factor (EGF, Invitrogen). We added the same amounts of bFGF and EGF every 3 days. After 7 days of culture, BMSC-derived spheres were collected and fixed with 4% paraformaldehyde (PFA) for 15 minutes. The characteristics of BMSC-derived spheres were examined by immunohistochemistry for nestin and Musashi-1. Anti-nestin rabbit polyclonal antibody (1:500; BD Biosciences, San Jose, CA) or anti-Musashi rabbit polyclonal antibody (1:500; Chemicon, Billerica, MA) was used as the primary antibody. Alexa Fluor 488-conjugated anti-mouse donkey IgG (1:1000; Molecular Probes, Eugene, OR) and Alexa Fluor 555-conjugated goat anti-rabbit IgG (1:1000; Molecular Probes) were used as the secondary antibodies. We counted the numbers of spheres and the number of marker-positive spheres in five randomly selected fields (3.4 mm^2 in area), and then calculated the ratio of nestin or Musashi-1 expressing spheres to the total number of spheres. Four independent cultures were performed.

In Vitro Neural Differentiation

To investigate the ability of BMSC-derived spheres to neurally differentiate, BMSC-derived spheres were plated onto 8-well chamber slides at a density of 100 spheres/well in serum-free DMEM/F-12 medium supplemented with B27, retinoic acid (1 mM, Sigma, St. Louis, MO), and dibutyryl cyclic adenosine monophosphate (AMP) (1 mM, Sigma). After 7 days of culture, the cells were fixed with 4% PFA for 15 minutes and immunostained for beta-III tubulin. Anti–beta-III tubulin rabbit polyclonal antibody (1:500; Sigma) was used as the primary antibody, and Alexa Fluor 488-conjugated anti-mouse donkey IgG (1:1000; Molecular Probes) was used as the secondary antibody. We counted the total numbers of the cells and the number of beta-III tubulin-positive cells in five randomly selected fields (3.4 mm^2 in area), and then calculated the ratio of beta-III tubulin expressing cells to the total number of cells. Four independent cultures were performed.

Transplantation Procedure

After labeling with DiI (Invitrogen, 5 μg/mL), the cell suspension of BMSC-derived spheres (10^5 cells in 10 μL DMEM) was injected into the cochlear modiolus of guinea pigs weighing 300 to 330 g as described previously.[10] Briefly, under general anesthesia with midazolam and xylazine, a small hole was made on the left otic bulla to expose the round window niche and the basal turn of the cochlea. After cochleostomy in the basal turn of the cochlea, a glass pipette, which was connected to a microsyringe (Hamilton, Reno, NV), was inserted into the cochlear modiolus of the basal portion of the cochlea. The glass pipette was removed 1 minute after completion of the infusion. Finally, the cochleostomy site was closed with a fat graft and then covered with fibrin glue.

BMSC-Derived Sphere Transplantation

BMSC-derived spheres were transplanted into intact or damaged cochleae of guinea pigs weighing 300 to 330 g. Four weeks after transplantation, four intact guinea pigs were transcardially perfused with phosphate buffered saline (PBS) at pH 7.4, followed by 4% PFA, and sacrificed under general anesthesia with an overdose of pentobarbital. The temporal bones were immediately dissected out and immersed in the same fixative for 4 hours at 4°C.

Ten guinea pigs received local application of ouabain (5 μL at a concentration of 5 mM in saline; Sigma), which causes SGN degeneration,[9] through the round window membrane under general anesthesia with midazolam and xylazine. One week after application, the electrically evoked auditory brainstem response (eABR), which has been used for functional evaluation of SGNs, was measured before cell transplantation as previously described.[10] Eight animals that showed no eABRs were used in the following experiments. Immediately after the eABR measurements, four animals received transplantation of BMSC-derived spheres similar to intact guinea pigs, and the other four animals received an injection of the culture media and were used as controls. Four weeks later, the cochlear specimens were collected after eABR recording.

Specimens (10-μm thick) were prepared using a cryostat after decalcification with 0.1 M ethylenediaminetetraacetic acid in PBS for 3 weeks at 4°C. Then, immunostaining for beta-III tubulin was performed, followed by nuclear staining with 4′,6-diamino-2-phenylindole dihydrochloride (DAPI; 2 μg/mL PBS, Molecular Probes). Specimens were viewed with a Leica TCS-SPE confocal laser-scanning microscope (Leica Microsystems Inc., Wetzlar, Germany). Five midmodiolar sections (each separated by 30 μm) were provided for quantitative analyses from each tissue sample. We defined the cells that were positive for DiI with a distinct nucleus identified by DAPI as surviving transplants. The numbers of transplants were counted in the internal auditory meatus and in five cochlear compartments (the modiolus, the scala vestibuli, the scala media, the scala tympani, and the lateral wall). We also counted the numbers of beta-III tubulin-positive transplants, and calculated the ratio of beta-III tubulin expressing transplants to total surviving transplants. In addition, the densities of SGNs in the Rosenthal canals were quantified in ouabain-treated specimens as described previously.[11] All data are presented as the mean ± 1 standard deviation.

Statistical Analyses

We statistically compared the total numbers of surviving transplants and the ratios for beta-III tubulin expression

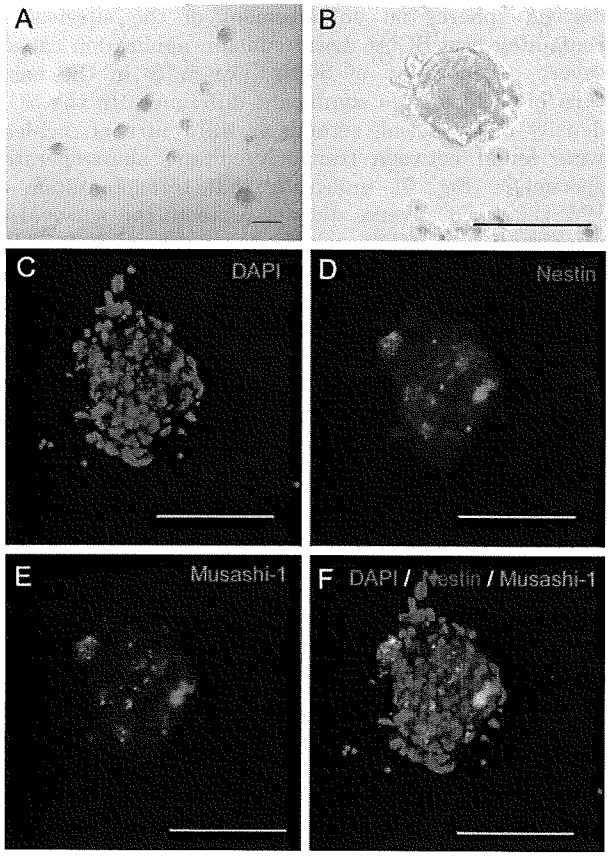

C O L O R

Fig. 1. BMSC-derived spheres. (A, B) Phase contrast images. (C) 4′,6-diamino-2-phenylindole dihydrochloride (DAPI) staining. (D) Immunostaining for nestin. (E) Immunostaining for Musashi-1. (E) Merged image. Scale bars = 500 μm.

between transplants in damaged cochleae and those in intact cochleae, using unpaired t tests. The difference in the locations of surviving transplants between damaged and intact cochleae was examined by two-way analysis of variance. In damaged models, the difference in the density of remaining SGNs between control and transplanted cochleae were compared using unpaired t tests. P values of $< .05$ were considered to be statistically significant.

RESULTS

Neural Induction of BMSCs

After 2 to 3 days in vitro, BMSCs began to form spheres. On day 7, $1.28 \pm 0.71 \times 10^4$ spheres were identified in each culture dish (Fig. 1A, 1B). Immunohistochemistry revealed the expression of nestin and Musashi-1 in the BMSC-derived spheres (Fig. 1C–1E). The expression of nestin was found in 91.9 ± 4.7% of total BMSC-derived spheres, and that of Musashi-1 was found in 93.6 ± 2.9%, suggesting that neurospheres were generated from guinea pig BMSCs.

F1

In Vitro Neural Differentiation

We transferred the BMSC-derived spheres into differentiation medium containing retinoic acid and dibutyryl cyclic AMP to examine their capacity for neural differentiation. Sphere-forming cells attached to culture dishes and the cells migrated from the sphere (Fig. 2A). Then, some of the cells extended processes (Fig. 2B). On day 7, 89.2 ± 2.8% of the cells expressed beta-III tubulin (Fig. 2C, 2D), indicating that BMSC-derived spheres have the capacity to differentiate into neurons.

F2

Transplantation Into Intact Cochleae

DiI-positive transplants were found in all intact cochleae following transplantation of BMSC-derived spheres. In each midmodiolar section, 74.1 ± 44.4 transplants were found. Transplants were located in multiple regions of the cochlea, predominantly in the scala tympani and the modiolus (Fig. 3A, 3C). Transplants were rarely found in the internal auditory meatus. The expression of beta-III tubulin was observed in 18.6% ± 6.4% of transplants (Fig. 3B).

F3

Transplantation Into Damaged Cochleae

DiI-positive transplants were also identified in all transplanted cochleae that had been damaged by ouabain. The number of surviving transplants in each midmodiolar section was 72.1 ± 53.1. There was no significant difference in the number of surviving transplants between intact and damaged cochleae, whereas the locations of surviving transplants in the damaged cochleae significantly differed from those in the intact cochleae ($P = .007$). In the damaged cochleae, the settlement of transplants was observed in the modiolus, similar to observations in the intact cochleae; however, the most prominent region for settlement of transplants

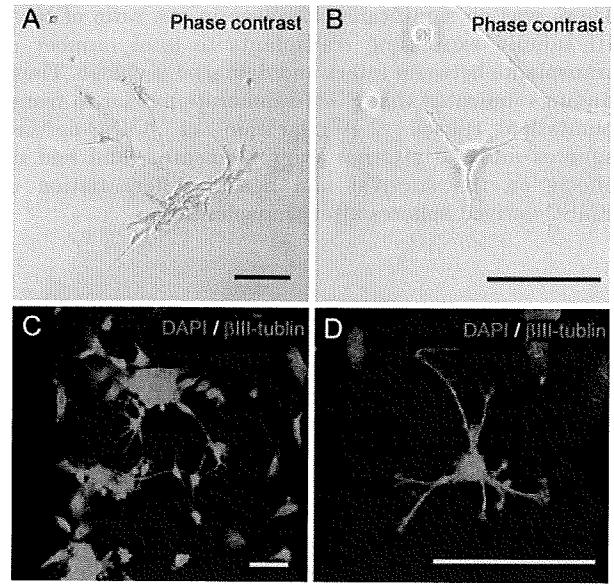

C O L O R

Fig. 2. Neural induction of BMSC-derived spheres in vitro. (A) Phase contrast image on day 3 in vitro. (B) Phase contrast image on day 7 in vitro. (C, D) Immunostaining for beta-III tubulin and nuclear staining with 4′,6-diamino-2-phenylindole dihydrochloride (DAPI). Scale bars = 20 μm.

AQ2

ID: thambikkanue | Black Lining: [ON] | Time: 17:19 | Path: N:/3b2/LARY/Vol00000/090467/APPFile/C2LARY090467

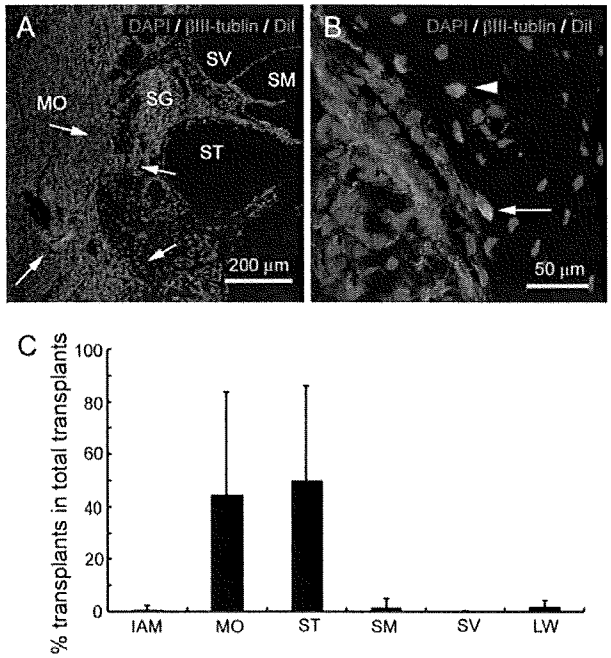

COLOR

Fig. 3. Transplantation into the intact cochleae. (A) Transplants labeled by DiI (red) are located in the modiolus (MO) of the cochlear basal portion (arrows). (B) Transplant labeled by DiI (arrow) is positive for beta-III tubulin and another (arrowhead) is negative. (C) The locations of transplants in the cochlea and in the internal auditory meatus (IAM). SV = scala vestibule; SG = spiral ganglion; SM = scala media; ST = scala tympani; LW = lateral wall. Bars represent a standard deviation.

F4 was the internal auditory meatus (Fig. 4A, 4C). The expression of beta-III tubulin was observed in 24.1 ± 5.3% of transplants in the damaged cochleae (Fig. 4B). There was no significant difference in the ratio of beta-III tubulin expressing transplants to total number of transplants between intact and damaged cochleae. These findings indicated that SGN degeneration prior to transplantation caused the migration of BMSC-derived spheres into the internal auditory meatus, and had no effects on the survival and neural differentiation of BMSC-derived spheres after transplantation.

Effects of Transplantation on Cochlear Function

We used eABR recording to monitor SGN function. All the animals receiving eABR evaluation showed no responses before an injection of a cell suspension or a culture medium. Four weeks postoperation, positive eABRs were identified in two of four animals in each group. Thresholds of eABRs in the two animals that showed positive responses in the transplanted group were 300 and 400 μA, and those in the sham-operated group were 250 and 650 μA. These findings indicated that transplantation of BMSC-derived spheres into the cochlear modiolus induced no significantly functional recovery of the cochlea.

We quantified SGN densities after cell transplantation or sham operation to evaluate the effects of BMSC-derived spheres on enhancement of the survival of remaining host SGNs. Local ouabain application caused severe degeneration of SGNs, especially in the basal turn of cochleae. No significant differences in the SGN density of the basal, second, or third turn of cochleae were found between transplanted and sham-operated specimens (Fig. 5), indicating that transplantation of F5 BMSC-derived spheres did not promote the survival of remaining host SGNs, which is consistent with eABR results.

DISCUSSION

The present findings demonstrate that guinea pig BMSCs are able to form spheres that have the capacity to differentiate into neurons in vitro. We aimed to replace SGNs, which are located in the cochlear modiolus, with BMSC-derived neurons. We thus directly injected BMSC-derived spheres into the modiolus of intact or damaged cochleae of guinea pigs. For accurate introduction of the cells into the cochlear modiolus, the size of the cochlea is a critical issue. Previously, we tried to introduce transplants into the cochlear modiolus of mice,[12] in which the success rate for the settlement of the transplants was not satisfactory. In addition, functional evaluation following cell transplantation is virtually impossible. On the other hand, guinea pig[10,13] or chinchilla[6] model systems exhibited better settlement

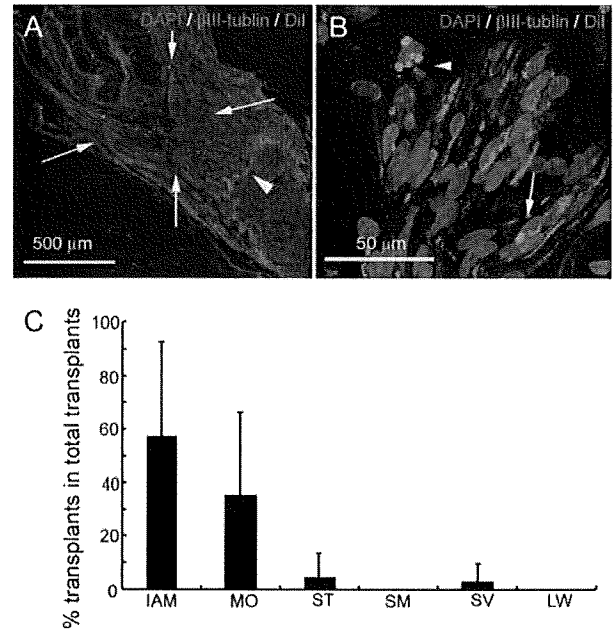

COLOR

Fig. 4. Transplantation into the damaged cochleae. (A) In the internal auditory meatus (IAM), transplants labeled by DiI (red) are observed (arrows). An arrowhead indicates the location of the glial-schwann junction. (B) A transplant labeled by DiI (arrow) is positive for beta-III tubulin and another (arrowhead) is negative. AQ4 (C) The locations of transplants in the cochlea and in the internal auditory meatus (IAM). MO = modiolus; ST = scala tympani; SM = scala media; SG = spiral ganglion; SV = scala vestibule; LW = lateral wall. Bars represent a standard deviation.

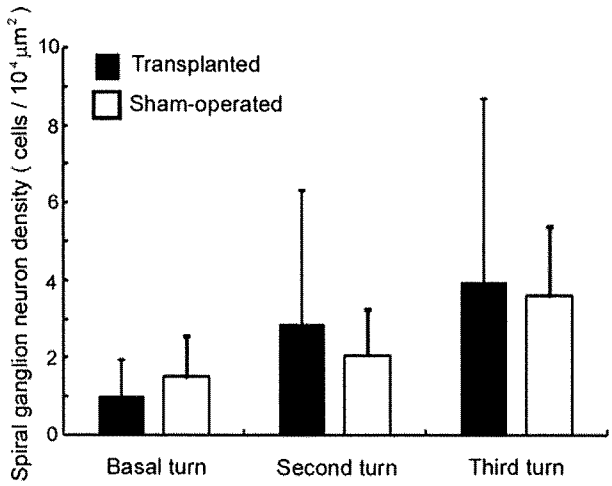

Fig. 5. Densities of remaining spiral ganglion neurons in the basal, second, or third turn of transplanted or sham-operated cochleae. There are no significant differences in the density of spiral ganglion neurons between transplanted and sham-operated cochleae.

of transplants in the cochlear modiolus and enabled functional evaluation using eABRs.[10,13] Moreover, our refined technique for cell introduction into the cochlear modiolus of guinea pigs caused no significant elevation of eABR thresholds.[10] Based on these previous findings, we used guinea pigs as experimental animals in the present study.

After transplantation of BMSC-derived spheres into the intact or damaged cochleae, BMSC-derived neurons were found in various portions of cochleae, including the cochlear modiolus. These findings indicate that BMSCs can be an alternative source of transplants for replacing SGNs. However, measurements of eABRs in the present study revealed no significant improvements of eABR thresholds after transplantation of BMSC-derived spheres. Previously, we demonstrated the recovery of eABR thresholds after transplantation of embryonic stem (ES) cell-derived neural progenitors in a different injury model.[13] There are several possible explanations for this lack of functional recovery following transplantation of BMSC-derived spheres. One is insufficient neurite elongation from BMSC-derived neurons to the central nervous system. Another possibility relates to different subtypes of neurons that are generated from BMSC-derived spheres. Previous studies have demonstrated that glutamatergic neurons are generated from both ES cells[14] and BMSCs,[15] meaning that both cell types have the capacity for differentiation into glutamatergic neurons. To achieve functional SGN restoration by transplantation of BMSC-derived spheres, additional treatments are required to enhance elongation of neurites from BMSC-derived neurons or to induce differentiation of BMSC-derived spheres into glutamatergic neurons.

Interestingly, the localization of transplants was different between the intact and damaged cochleae. In the intact cochleae, a number of transplants were found in the scala tympani. We injected BMSC-derived spheres through the scala tympani.[10] Therefore, transplants that were found in the scala tympani may have originated from the leakage of injected cell suspensions. In the intact cochlea, there are limited spaces in the cochlear modiolus, because host SGNs and auditory nerves are present, which may cause the leakage of injected cell suspensions into the scala tympani. On the other hand, the loss of host SGNs may result in an increase of spaces for transplants in the cochlear modiolus. Hence, in the damaged cochleae limited numbers of transplants were observed in the perilymphatic spaces including the scala tympani. In the damaged cochleae a number of transplants were found not only in the cochlear modiolus but also in the internal auditory meatus. Transplants in the internal auditory meatus may migrate from the cochlear modiolus, which is an injected site. The degeneration of SGNs could make a path from the cochlear modiolus of the basal portion to the internal auditory meatus, or stimulate production of chemotactic factors that promote the migration activity of BMSC-derived spheres. Future studies should be performed to determine the mechanisms of migration of BMSC-derived spheres into the internal auditory meatus.

CONCLUSION

The present findings demonstrate that BMSCs are a preferable source of neurospheres and that BMSC-derived spheres retain the ability for neural differentiation after transplantation into the cochlea. Functional restoration of damaged cochleae was not achieved by transplantation of BMSC-derived spheres, although a number of transplant-derived neurons settled in the cochlea and in the internal auditory meatus. To achieve functional restoration of SGNs by transplantation of BMSC-derived spheres, additional treatments including local application of neurotrophic or growth factors may be required.

BIBLIOGRAPHY

1. Coleman B, De Silva MG, Shephered RK. The potential of stem cells for auditory neuron generation and replacement. *Stem Cells* 2007;25:2685–2694.
2. Nakagawa T, Ito J. Cell therapy for inner ear diseases. *Curr Pharm Des* 2005;11:1203–1207.
3. Li H, Corrales CE, Edge A, Heller S. Stem cells as therapy for hearing loss. *Trends Mol Med* 2004;10:309–315.
4. Kitada M, Dezawa M. Induction system of neural and muscle lineage cells from bone marrow stromal cells; a new strategy for tissue reconstruction in degenerative diseases. *Histol Histopathol* 2009;24:631–642.
5. Liu ZJ, Zhuge Y, Velazquez OC. Trafficking and differentiation of mesenchymal stem cells. *J Cell Biochem* 2009;106: 984–991.
6. Naito Y, Nakamura T, Nakagawa T, et al. Transplantation of bone marrow stromal cells into the cochlea of chinchillas. *Neuroreport* 2004;15:1–4.
7. Matsuoka AJ, Kondo T, Miyamoto RT, Hashino E. In vivo and in vitro characterization of bone marrow-derived stem cells in the cochlea. *Laryngoscope* 2006;116:1363–1367.
8. Sharif S, Nakagawa T, Ohno T, et al. The potential use of bone marrow stromal cells for cochlear cell therapy. *Neuroreport* 2007;18:351–354.

ID: thambikkanue | Black Lining: [ON] | Time: 17:19 | Path: N:/3b2/LARY/Vol00000/090467/APPFile/C2LARY090467

9. Matsuoka AJ, Kondo T, Miyamoto RT, Hashino E. Enhanced survival of bone-marrow-derived pluripotent stem cells in an animal model of auditory neuropathy. *Laryngoscope* 2007;117:1629–1635.
10. Ogita H, Nakagawa T, Lee KY, et al. Surgical invasiveness of cell transplantation into the guinea pig cochlear modiolus. *ORL J Otorhinolaryngol Relat Spec* 2009;71:32–39.
11. Kada S, Nakagawa T, Ito J. A mouse model for degeneration of the spiral ligament. *J Assoc Res Otolaryngol* 2009; 10:161–172.
12. Tamura T, Nakagawa T, Iguchi F, et al. Transplantation of neural stem cells into the modiolus of mouse cochleae injured by cisplatin. *Acta Otolaryngol* 2004; (suppl 551): 65–68.
13. Okano T, Nakagawa T, Endo T, et al. Engraftment of embryonic stem cell-derived neurons into the cochlear modiolus. *Neuroreport* 2005;16:1919–1922.
14. Reyes JH, O'Shea KS, Wys NL, et al. Glutamatergic neuronal differentiation of mouse embryonic stem cells after transient expression of neurogenin 1 and treatment with BDNF and GDNF: in vitro and in vivo studies. *J Neurosci* 2008;28:12611–12631.
15. Kondo T, Johnson S, Yoder M, et al. Sonic hedgehog and retinoic acid synergistically promote sensory fate specification from bone marrow-derived pluripotent stem cells. *Proc Natl Acad Sci U S A* 2005;102:4789–4794.

AQ1: adenosine monophosphate (AMP) okay?

AQ2: Please note spelling of tubulin in Figure 2 (tublin).

AQ3: Note spelling of tubulin in Figure 3 (tublin).

AQ4: Note spelling of tubulin in Figure 4 (tublin).

Journal of Biomechanical Science and Engineering

Vol. 5, No. 3, 2010

Culturing Neurons on MEMS Fabricated P(VDF-TrFE) Films for Implantable Artificial Cochlea*

Hirofumi SHINTAKU**, Takashi TATENO**, Nobuyoshi TSUCHIOKA**, Harto TANUJAYA**, Takayuki NAKAGAWA***, Juichi ITO*** and Satoyuki KAWANO**

**Department of Mechanical Science and Bioengineering, Graduate School of Engineering Science, Osaka University, Machikaneyama-cho 1-3, Toyonaka, Osaka 560-8531, Japan
E-mail: shintaku@me.es.osaka-u.ac.jp

***Department of Otolaryngology, Head and Neck Surgery, Graduate School of Medicine, Kyoto University, Kawahara-cho 54,Shogoin, Sakyo-ku, Kyoto 606-8507, Japan

Abstract

In this paper, we report an *in vitro* study on the biocompatibility of poly(vinylidene fluoride-trifluoroethylene) (P(VDF-TrFE)) films for the implantable artificial cochlea. The implantable artificial cochlea comprises a piezoelectric membrane made of P(VDF-TrFE), platinum (Pt) thin film electrodes, and a silicon substrate which are designed to stimulate neurons in a cochlea and fabricated by microelectromechanical systems (MEMS) and thin film technologies. The biocompatibility of P(VDF-TrFE) film is evaluated by culturing cerebral cortical neurons from rats on it. The fibronectin from human plasma and the collagen from the calf skin are used as the cell adhesion factors. Since neurons extend dendrites and axons from the somata, it is found that the neurons are successfully cultured on the surface of P(VDF-TrFE) films modified both by the fibronectin and by the collagen. Furthermore, it is also found that the neurons are also successfully cultured over the Pt electrode on the P(VDF-TrFE) of the implantable artificial cochlea modified by the fibronectin. Consequently, the biocompatibility and the applicability of the MEMS fabricated P(VDF-TrFE) films and the implantable artificial cochlea are confirmed.

Key words: Biocompatibility, MEMS, Cerebral Cortical Neuron, Medical Equipment, Biomechanical Engineering, Piezoelectric Device

1. Introduction

Piezoelectric materials are promising ones in the field of implantable artificial organs, since they can be used for electric power generators and sensors using the direct piezoelectric effect and for actuators using the inverse piezoelectric effect. For instance, Lewandowski et al.[1] proposed a piezoelectric power generator with a muscle-tendon unit. Platt et al.[2] proposed a self-powered embedded sensor for orthopedic implants. Schubert et al.[3] and Schrag et al.[4] proposed micropumps using piezoelectric actuators for an implantable artificial pancreas and artificial bowel sphincter, respectively. Furthermore, authors have proposed a piezoelectric artificial cochlea which realizes the acoustic/electric conversion and the frequency selectivity without an externally supplying energy[5]-[7].

Figure 1 shows a schematic of implantable artificial cochlea we have proposed. The

*Received 13 June, 2009 (No. 09-0262)
[DOI: 10.1299/jbse.5.229]

device comprises a piezoelectric membrane (ABM) made of poly(vinylidene fluoride-trifluoroethylene) (P(VDF-TrFE)) and discrete electrodes made of platinum (Pt) thin films, which are fabricated on a silicon (Si) substrate by microelectromechannical systems (MEMS) and thin film technologies. When the curved ABM is extended straight, it can be seen that ABM has a trapezoidal shape. The shape which is designed to mimic the biological system, i.e. the basilar membrane in cochlea, enables to analyze the frequency of acoustic wave. To cure the sensorineural hearing loss in the future, the implantable artificial cochlea is inserted into a cochlea which is filled with lymph fluid. ABM in the cochlea is vibrated by externally applying acoustic waves which is transmitted through the outer ear and the middle one. The mechanical deformation of ABM due to the vibration is converted to electric signals by the piezoelectric effect of P(VDF-TrFE) and the electric signals stimulate neurons in the cochlea. Since the proposed device is basically developed by microfabrication technologies, the electrodes can be easily integrated and their number can be increased, whereas the conventional system is limited by the relatively small number of electrodes as 12-22[8]-[10]. Furthermore, since the frequency of acoustic wave is analyzed by a biomimetic system, the device may realize more "natural hearing" compared with the conventional system.

The basic mechanisms of frequency analysis and acoustic/electric conversion have been studied using a prototype device fabricated by bulk processes[5],[6]. The effects of surrounding fluid of ABM have been studied by the comparison between theoretical results and experimental ones[6]. Furthermore, for the miniaturization of device and the amplification of electric signals, a fabrication process based on MEMS and thin film technologies have been developed[7]. Although the ultimate goal of our studies is to develop the fully self-contained implantable artificial cochlea, the biocompatibility of device has not been discussed. Since Si and Pt are relatively popular materials in the MEMS field, there are literatures that discuss their biocompatibility[11]. However, as far as authors are aware, there are few papers that evaluate the biocompatibility of P(VDF-TrFE) films fabricated by MEMS processes.

Thus, in this paper, we investigate the biocompatibility of P(VDF-TrFE) films for the proposed artificial cochlea in terms of cytotoxicity. To transfer the electric signal from Pt electrodes to auditory neurons in the cochlea over the P(VDF-TrFE) thin film, the neurons should be cultured or at least they should extend neurites on P(VDF-TrFE) films. Therefore, the *in vitro* experiment is carried out by culturing cerebral cortical neurons from rats on the P(VDF-TrFE) films. The cultured neurons are labeled by the fluorescent Nissl stain and observed by a fluorescent microscope. To observe the detailed configurations of neurons by the phase contrast microscope, P(VDF-TrFE) films are also fabricated on glass substrates, instead of Si substrates. Since MEMS fabricated P(VDF-TrFE) films can be applied to develop other biomedical devices, the results obtained here provide not only the fundamental knowledge on the biocompatibility of proposed artificial cochlea but also on that of P(VDF-TrFE) films for other artificial organs.

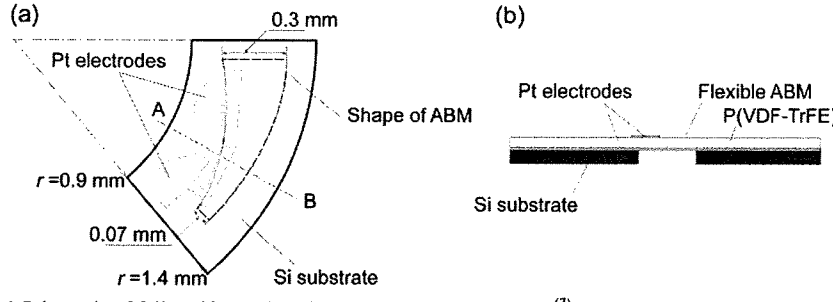

Fig. 1 Schematic of fully self-contained implantable artificial cochlea[7]; (a) top view and (b) cross sectional view at AB of (a).

2. Materials and methods

The fabrication process of implantable artificial cochlea is described as follows. The surface of Si substrate (100) is pretreated by hexamethyldisilazane (OAP, Tokyo Ohka Kogyo) to enhance the adhesion of P(VDF-TrFE) film. Then, a N,N-dimethylformamide (DMF) solution including P(VDF-TrFE) (KF-W#2200 P(VDF-TrFE), KUREHA) at the concentration of 8.0 wt% is spun on the substrate. The substrate is heated on a hotplate at 50 °C for 12 hours to evaporate DMF and at 145 °C for 2 hours to crystallize P(VDF-TrFE). The Pt electrodes are fabricated on the P(VDF-TrFE) film using a lift off process. The etching process of Si which makes the P(VDF-TrFE) film to be a flexible ABM is omitted in this study, since that is not necessary to discuss the biocompatibility. For the purpose of optical observation using a phase contrast microscope, glass substrates (Micro slide glass, Matsunami) are also used to fabricate P(VDF-TrFE) films instead of Si substrates.

A piece of processed substrate is sterilized by spraying with 70 % ethanol and is put into tissue culture dishes made of polystyrene. Then, the surfaces of substrates are modified by cell adhesion factors. Since it is obvious that the adherent cells have difficulties in growing on the hydrophobic surfaces such as P(VDF-TrFE), two types of popular cell adhesion factors, the fibronectin from the human plasma[12] and the collagen from the calf skin[13], are used to focus the discussion on the cytotoxicity of the material. The process of surface modification is briefly described as follows. For the modification by fibronectin, the substrate is immersed in phosphate buffered saline (PBS) containing fibronectin (F0895, Sigma Aldrich Japan) at the concentration of 6.7×10^{-3} g/ml and is incubated at room temperature for more than 45 min. After that, the residual solution is removed. On the other hand, for the modification by the collagen, the substrate is immersed in 0.1 M acetic acid containing 0.1 wt% collagen (C8919, Sigma Aldrich Japan) and is incubated at 4 °C for 12 hours. After removing the residual solution, the substrate is kept at room temperature to be dried for 12 hours.

Dulbecco's modified Eagle's medium (DMEM, Gibco) which contains fetal bovine serum of 5.0 vol%, horse serum of 5.0 vol%, penicillin of 6.2×10^{-4} g/ml, and insulin of 3.5×10^{-5} g/ml[14] is poured into the tissue culture dish which contains the surface modified substrate. Then, the DMEM containing dissociated cerebral cortical neurons from rats at postnatal day 1 is introduced to the dish. Since it is quite difficult to obtain enough amounts of neurons from a cochlea, cerebral cortical neurons are used. However, the results are applicable to discuss the biocompatibility as a first step. The dish is placed in an incubator which is maintained at 37 °C and 5% CO_2 to culture neurons on the substrates for 3 days. After culturing 3 days, the neuron is fixed by 4% paraformaldehyde and labeled by fluorescent Nissl stains (NeuroTrace™ 500/525 green, Sigma Aldrich Japan)[15] for the subsequent optical observation. Since the Nissl substance labeled by the stain is abundant in neurons, cells with high fluorescent intensity indicate neurons. The viability is evaluated based on the morphology of cells observed by the fluorescent microscope and the phase contrast one. Although most of cells used here are neurons, cells include some glia ones. Thus, the neurons are distinguished based on the observations using both fluorescent photographs and phase contrast ones.

3. Results and discussion

Figures 2 (a), (b), and (c) show a phase contrast photograph, a fluorescent one, and a merged one of Figs. 2(a) and 2(b), respectively, observed at a same place of P(VDF-TrFE) fabricated on the glass substrate and modified by the fibronectin. Since the P(VDF-TrFE) and the glass substrate are transparent, it is possible to observe neurons, dendrites, and axons using a phase contrast microscope as shown in Fig. 2(a). Symbols of Ss and Ds in Fig. 2(a) are considered as somata and dendrites which adhere on the substrate, respectively,

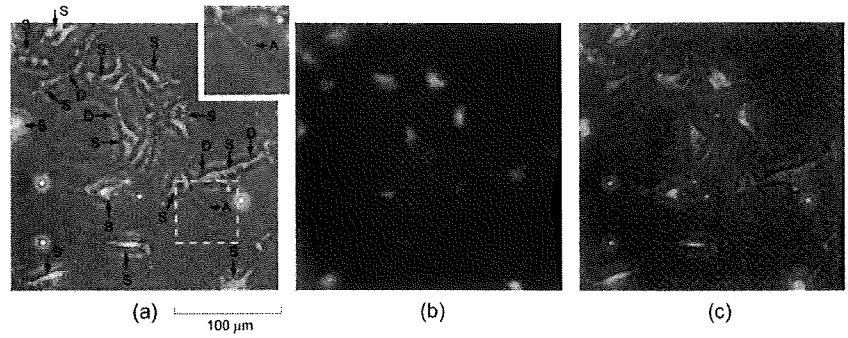

Fig. 2 (a) Phase contrast photograph, (b) fluorescent one, and (c) merged one of (a) and (b) of cultured neurons over P(VDF-TrFE) film modified by fibronectin and fabricated on glass substrate. Symbols A, D, and S indicate axon, dendrite, and soma, respectively. Inset in (a) is enlarged view around axon of A.

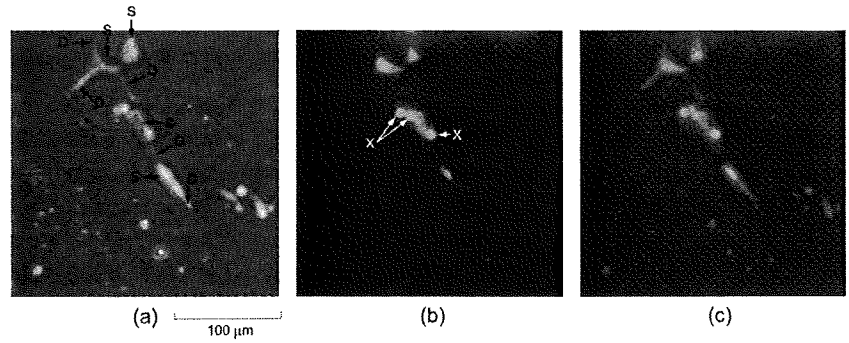

Fig. 3 (a) Phase contrast photograph, (b) fluorescent one, and (c) merged one of (a) and (b) of cultured neurons over P(VDF-TrFE) film modified by collagen and fabricated on glass substrate. Symbols D, S, and X indicate dendrite, soma, and dead cell, respectively.

since the stained areas in Fig. 2(b) correspond to the place of somata and dendrites as shown in Fig. 2(c). Furthermore, symbol A in the inset of Fig. 2(a) must be an axon. From these observation, it can be said that the neurons are successfully cultured on the P(VDF-TrFE) film modified by the fibronectin.

Figures 3 (a), (b), and (c) show a phase contrast photograph, a fluorescent one, and a merged one of Figs. 3(a) and 3(b), respectively, observed at a same place of P(VDF-TrFE) fabricated on the glass substrate and modified by the collagen. Symbols of Ss and Ds in Fig. 3(a) indicate somata and dendrites, respectively, where it is confirmed by the fluorescent photograph of Fig. 3(b) and by the merged one of Fig. 3(c). From the fluorescent photograph of Fig. 3(b), it is possible to roughly evaluate the viability of neurons based on the shapes of stained areas, where living and dead neurons seem to be distorted shapes and circular shapes, respectively. Xs in Fig.3 (b) must be dead neurons which are approximately circular shape. However, since most neurons are living and extend dendrites, it can be said that neurons are successfully cultured on the P(VDF-TrFE) film modified by the collagen. As shown in Figs. 2 and 3, the qualitative difference in terms of viability of neurons is not found between the cell adhesion factors of the fibronectin and the collagen. Consequently, it is found that P(VDF-TrFE) is applicable to a biocompatible material in terms of culturing neurons on it.

Figure 4 shows fluorescent photographs of cultured neurons over the P(VDF-TrFE) film fabricated on a Si substrate and modified by the fibronectin, that is, our proposed implantable artificial cochlea. The relatively dark background at the right half of Fig. 4 (a) indicates the Pt electrode on the P(VDF-TrFE) film. Since the Si substrate is not transparent, the evaluation on the cell viability is carried out based on this fluorescent